Quaternary Science Reviews 210 (2019) 190–210

Contents lists available at ScienceDirect

Quaternary Science Reviews

journal homepage: www.elsevier.com/locate/quascirev

Palaeoenvironmental and palaeohydrological variability of mountain areas in the central Mediterranean region: A 190 ka-long chronicle from the independently dated Fucino palaeolake record (central Italy)

G. Mannella [a, *], B. Giaccio [b], G. Zanchetta [a], E. Regattieri [a, c], E.M. Niespolo [d, e], A. Pereira [f, g, h], P.R. Renne [d, e], S. Nomade [f], N. Leicher [i], N. Perchiazzi [a], B. Wagner [i]

[a] Dipartimento di Scienze della Terra, University of Pisa, Pisa, Italy
[b] National Research Council, Institute of Environmental Geology and Applied Geoengeneering (IGAG-CNR), Rome, Italy
[c] National Research Council, Institute of Earth Sciences and Georesources (IGG-CNR), Pisa, Italy
[d] Department of Earth and Planetary Science, University of California, Berkeley, USA
[e] Berkeley Geochronology Center, Berkeley, USA
[f] Laboratoire des Sciences du Climat et de l'Environnement (CEA-CNRS-UVSQ), Gif-sur-Yvette, France
[g] Ecole française de Rome, Rome, Italy
[h] UMR 7194 HNHP, National Museum of Natural History, Paris, France
[i] University of Cologne, Institute of Geology and Mineralogy, Cologne, Germany

ARTICLE INFO

Article history:
Received 8 October 2018
Received in revised form
18 February 2019
Accepted 27 February 2019
Available online 16 March 2019

Keywords:
Pleistocene
Central Mediterranean
Palaeolimnology
Environmental change
Glacial-interglacial cycles
$^{40}Ar/^{39}Ar$ tephrochronology
Biogeochemistry

ABSTRACT

Proxy records of past climate change spanning beyond the radiocarbon range commonly derive their chronologies from orbital tuning strategies, thus bounding our spatio-temporal reconstructions to *a priori* assumptions that can not be directly tested. Here we present a tephrochronologically constrained framework of past environmental and climatic changes in the central Mediterranean region during the last ca. 190 ka. Our research is based on a high-resolution, multi-proxy study of a sedimentary record (cores F1-F3) retrieved from the Fucino Basin lacustrine succession, central Italy, in 2015. We update the existing tephrostratigraphic framework of the F1-F3 record with the finding of the widespread Campanian Ignimbrite tephra marker layer and produce a robust and independent chronology based on new and published $^{40}Ar/^{39}Ar$ and ^{14}C dating of 17 tephra layers. Observed palaeoenvironmental changes are tracked in other lacustrine, marine and speleothem records across the Mediterranean and North Atlantic regions via tephrostratigraphic correlations and chronological matching providing a robust assessment of age uncertainties. Results show a complex interplay between local environmental changes and broad-scale climatic processes highlighting a strong orbital forcing on glacial-interglacial changes. Along with these major changes we detect prominent millennial-scale variability. During times of intermediate global ice volumes, Mediterranean mountain ecosystems oscillated around an “interglacial” state suggesting that climatic shifts, although large, did not exceed the local environmental tolerance-resilience threshold. Conversely, during periods of large global ice volume, we observe subdued millennial-scale variability with ecosystems operating in a strictly ruled glacial environment.

1. Introduction

Current knowledge of past environmental and hydrological variability in the Mediterranean region has been gained through the analysis of discontinuous lacustrine successions, speleothem records (e.g., Roberts et al., 2008; Regattieri et al., 2014, 2015; Drysdale et al., 2004, 2005, 2007, 2009) and marine sediment cores (e.g., Toucanne et al., 2015). However, aside from U-Th dated speleothems, chronologies of these archives are based on various dating approaches, most of which depend on *a priori* assumptions on how different proxy data respond to variations in latitudinal distribution of incoming solar radiation as modulated by the change in Earth's orbital geometry. This unavoidably introduces substantial uncertainties, especially when comparing climatic

* Corresponding author.
E-mail address: giorgio.mannella@dst.unipi.it (G. Mannella).

https://doi.org/10.1016/j.quascirev.2019.02.032
0277-3791/

events at millennial-scale or shorter time-scales in different records. (Govin et al., 2015; Zanchetta et al., 2016). Indeed, most of the chronologies of sedimentary records spanning beyond the ~45 ka limit of radiocarbon (^{14}C) dating rely on aligning distinctive climato-stratigraphic features with reference records. These latter records are often dated by similar orbital tuning strategies (e.g., Lisiecki and Raymo, 2005).

As a result, the choice of different reference records can lead to age discrepancies of several thousand years and to inconsistencies in the aligned chronologies (e.g., Govin et al., 2015). Thus, despite the growing number of climatic archives investigated around the globe, chronology is still the Achilles' heel of many palaeoclimatic reconstructions. At its current stage of development, chronology often limits the assessment of age, rates of change, duration of events, leads and lags of various parameters and, more generally, our understanding of the role of different processes and mechanisms in driving observed changes (e.g., Zanchetta et al., 2016).

It is therefore of primary importance to define an accurate chronography of past climate variations based on radioisotopically-dated time series from which tie points between terrestrial, marine and ice-core palaeoclimate records can be unambiguously drawn. The high climatic-sensitivity (Giaccio et al., 2015a; Regattieri et al., 2015; Zanchetta et al., 2017a) and the rich content in volcanic ash (Giaccio et al., 2012, 2017a) of Quaternary lacustrine successions hosted in the intermountain basins of the Central Apennine make these archives particularly suitable for addressing palaeoclimatological issues within an independent and consistent chronological framework provided by direct or indirect $^{40}Ar/^{39}Ar$ dating. Among these, the Fucino Basin (Fig. 1) lacustrine sedimentary succession offers the unique opportunity to continuously record and independently date past climate changes in the central Mediterranean Region over a long Quaternary time interval, possibly spanning the last ~2 Ma (Giaccio et al., 2015a).

Here we present a multi-proxy high-resolution and tephrochronologically dated lacustrine record from the Fucino Basin. The record provides a chronologically well constrained reconstruction of regional climate and environmental evolution over the last ca. 190 ka. We then compare our record with other key regional and extra-regional archives (Fig. 1a) with the aim to define forcing mechanisms and climatic teleconnections within a robust chronological framework.

2. Geological setting and general background

The Fucino Basin (42.00°N, 13.56°E) is located in the Abruzzo region (Central Italy), about 80 km from both the Tyrrhenian and Adriatic coasts and is the largest (ca. 900 km^2) late Neogene – Quaternary intermountain sedimentary basin of the Central Apennines orogenic belt (Galadini and Messina, 2004). In this sector of the chain the geology is dominated by the Lazio-Abruzzo inner to outer shelf carbonates (Triassic - middle Miocene), with minor outcrops of syn-orogenic units made up of calcirudites grading upwards to siliciclastic flysches (Latest Miocene – Early Pliocene). These are unconformably overlain by Plio-Quaternary terraced alluvial and lacustrine deposits. The Plio-Quaternary Units are divided into Lower (Pliocene - Lower Pleistocene) and Upper (Middle Pleistocene - Holocene) Units by a major stratigraphic unconformity. Lower and Upper Units show a prominent change in detrital provenance which testifies the progressive transition from an early geological landscape, dominated by siliciclastic lithotypes, to the actual landscape mainly carved in limestone lithotypes (Bosi et al., 1995; Cavinato et al., 2002). The Fucino Basin is bounded by the Fucino Fault System (FFS), a complex framework of normal and oblique-slip extensional faults (Cavinato et al., 2002). Active since the Pliocene, the FFS is one of the most active seismogenetic structures of the Central Apennine and has been responsible for repeated catastrophic earthquakes in historic times (last event: Avezzano earthquake, 1915, Mw = 7.0; e.g., Galli et al., 2016). The long-term interplay between transtensive activity along the FFS and regional uplift, has produced a great half-graben basin with a steep topographic gradient between the basin floor (ca. 650–1050 m a.s.l.) and its flanks bounded by high reliefs (up to 2486 m a.s.l.). Differential movements along fault sectors of the FFS controlled the sedimentary infilling of the basin, on the one hand, by generating sediment accommodation space and, on the other hand, by continuously rejuvenating relief energy and recycling older sedimentary successions (Giraudi, 1988, 1989; Cavinato et al., 2002 for a detailed discussion). The continued basin expansion along with subsidence in the western sector of the basin led to the transition from overfilling to underfilling in the late Pliocene-early Pleistocene. This is reflected by the shift from an initial stage dominated by fluvial processes to a later stage dominated by lacustrine environments (Cavinato et al., 2002). Since the early Pleistocene, Lake Fucino occupied the lowermost part of the basin allowing the continuous deposition of fine-grained lacustrine calcareous marls, fluvio-glacial sediments from the surrounding highlands (Frezzotti and Giraudi, 1992) and several tephra layers from peri-Tyrrhenian magmatic provinces (Giaccio et al., 2015a, 2017a; Di Roberto et al., 2018). Prior to its artificial drainage in 1875, Lake Fucino was Italy's third largest lake. It had a mean extension of 140 km^2 and average maximum depth of 20 m (Giraudi, 1989). The lake received waters from a network of small streams draining a 710 km^2 wide catchment and from a wide karstic system developed from the Meso-Cenozioc carbonates. As the lake had no natural outflow stream, lake levels were directly linked with the local hydrogeological regime (Giraudi, 1990, 1998). There are strong evidences for large lake-level oscillations on both secular and millennial time scales (Giraudi, 1989, 1998). Up to historical times, maximum lake levels where partially stabilised by karstic swallow holes located along the southwestern edge of the basin (Giraudi, 1989) and by a drainage tunnel built during the 1st century CE by the Romans.

2.1. Local climatic setting

Historic data (1951–2000) from the regional meteorological network indicate that Fucino Basin has a warm-summer Mediterranean (Csb *sensu* Köppen, 1918) climate locally showing continental characteristics (i.e., more humid summers and/or colder winters). Monthly average temperatures remain above 10 °C between May and September reaching their maximum between July and August (from 18 to 21 °C) and their minimum in January (from −5 to −2 °C). Measured temperature extremes are 41 °C and −32 °C at the Borgo Ottomila meteorological station, located near the geographical center of the basin.

Mean annual precipitation ranges from 600 to 750 mm/a in the plain area and from 900 to 1200 mm/a across the piedmont belt. Precipitation is unevenly distributed throughout the year with a progressive decrease from autumn (ca. 33%) through winter (ca. 31%), spring (ca. 23%) and summer (ca. 13%). Snow fall is common in the winter season, can affect the whole altitudinal range of the basin, and is abundant at altitudes of more than 1000 m a.s.l. Here the ground usually remains snow-covered for at least two months. Mathematical simulations by Tomassetti et al. (2003) on the local climatic influence of Lake Fucino suggest that, prior to its drainage, the lake exerted a strong influence on the local climate by reducing the strength of extreme events. However, its influence on annual average temperatures and precipitations may have been negligible.

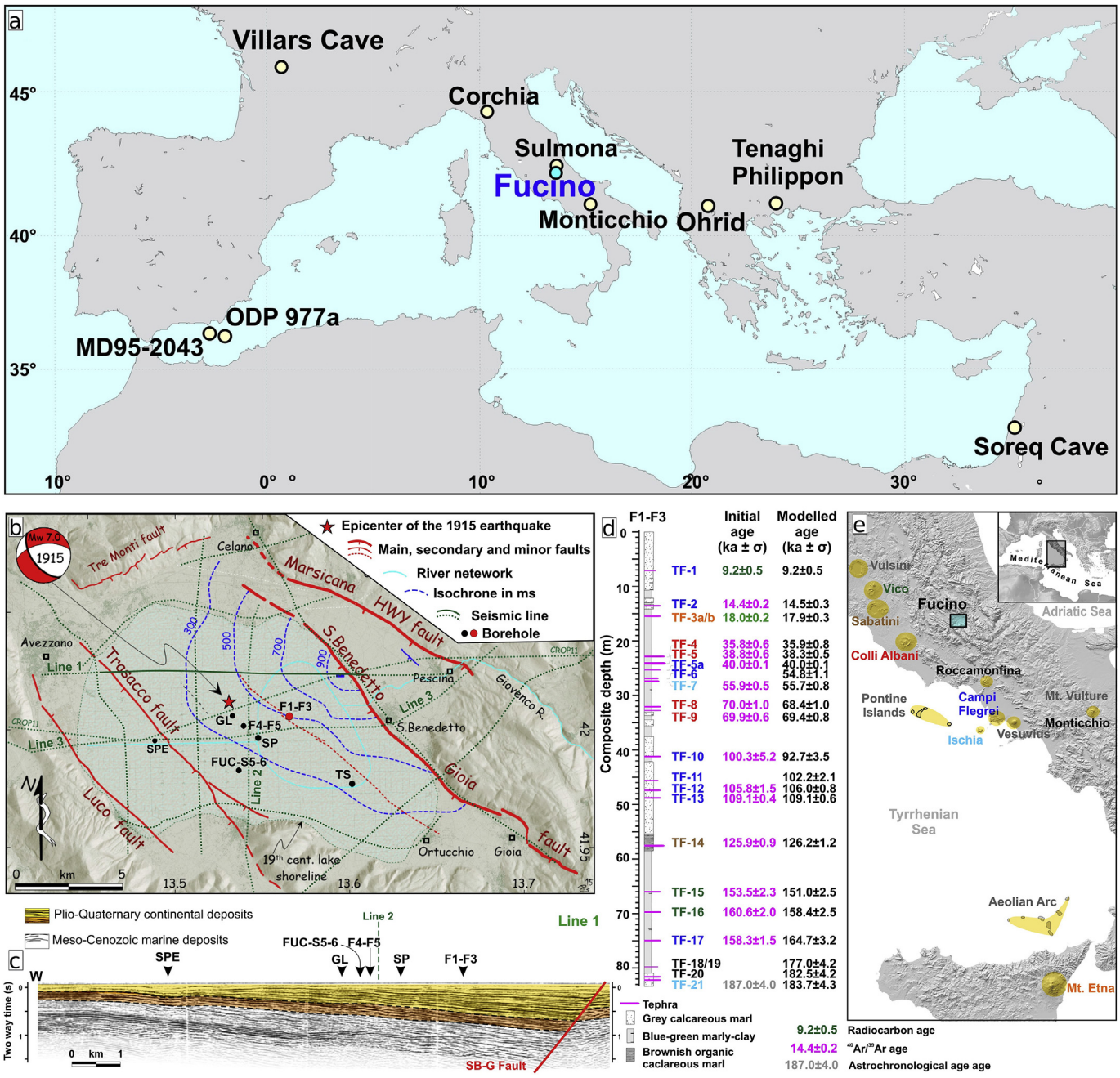

Fig. 1. Reference map – (a) Map of the Mediterranean region displaying the Fucino Basin and other selected records. (b) Shaded relief map showing the location of the GL, TS, SP, F1-F3 (Giaccio et al., 2015a,b, 2017a,b, this study), F4-F5 (Mannella et al., 2018), FUC-S5-6 (Di Roberto et al., 2018) boreholes. Dashed blue lines represent isochrones (in ms) of the Plio-Quaternary sedimentary infilling, bold red lines represent Quaternary master faults responsible for the asymmetrical (half-graben) basin geometry. Dotted green lines represent traces of the available seismic lines. (c) Seismic line 1 (see trace in panel b) showing the internal architecture of the Plio-Quaternary continental deposits of the Fucino Basin along a W-E oriented profile. The projected location of various boreholes is also shown. (d) Schematic stratigraphic log of core F1-F3 with an updated tephrostratigraphic and chronological framework (this study). Tephra layer labels use the same colour key as in panel "e" to indicate different volcanic sources. (e) Location of Fucino Basin with respect to the main eruptive centres active during the last 1.8 Ma. (For interpretation of the references to colour in this figure legend, the reader is referred to the Web version of this article.)

3. Material and methods

3.1. Core composite

The Fucino F1-F3 core was drilled in June 2015 from the depocentral area of the basin (Fig. 1b and c). Details on coring techniques, boreholes location and procedures for creating the composite profile have been described by Giaccio et al. (2015a). Briefly, the F1-F3 sedimentary succession originates from two parallel boreholes of 60.75 m and 80.27 m depth, respectively. As overlap was not possible below 60.75 m, the lower part of the core composite displays 20–25 cm gaps every 1.5 m. For the present study, the original composite was carefully re-examined with particular attention to gaps in the overlapping section between the F1 and F3 core series. This operation resulted in a lengthening of 43 cm of the original core composite (total length 82.70 m). The core composite was further elaborated by removing tephra layers thicknesses from the total depth prior to the age modelling

procedure. The tephra-free core composite depth is provided as meters below basin floor (m bbf composite).

3.2. Subsampling and analyses on discrete samples

The core composite was subsampled at the Istituto di Geologia Ambientale e Geoingegneria of the Italian National Research Council (IGAG-CNR) in Rome by taking a 1 cm-thick slice of sediment on every 4th cm of the tephra-free core composite and resulted in 1800 samples. Samples where then dried in an oven for 72 h at 50 °C at the Department of Earth Sciences of the University of Pisa. For the present study a subset of 1136 samples with a variable resolution (normal resolution 1 every 8th cm, and enhanced resolution, i.e. 1 every 4th cm, from 0 to 4.97 m and from 22.41 to 38.66 m bbf) was finely hand-ground with an agate mortar and pestle for further analyses.

3.3. X-ray powder diffraction analyses

63 unevenly spaced samples taken from the F1-F3 core composite and 7 samples of terraced fluvial sediments from Giovenco river, the main tributary of the Fucino Basin, were analysed for their bulk mineralogical composition. Samples were reduced to fine powders ($\phi < 10\,\mu m$) by hand-grinding in an agate mortar with acetone. Randomly oriented powder samples were analysed using a Bruker D2 Phaser diffractometer (University of Pisa, Department of Earth Sciences). Analyses were run at room temperature using a Cu X-ray source operating at 30 kV and 10 mA coupled with a Ni filter and a fixed 0.2° divergence slit. Incremental step size was 0.01° and 2θ was between 4 and 65°. Diffractograms were processed with the DiffracEva software, allowing the identification of the main mineralogical phases and the estimation of the relative abundances of calcite to quartz by comparing peak areas of the two phases.

3.4. Biochemical analyses

A total of 1136 samples were analysed for total nitrogen (TN), total organic (TOC) and inorganic (TIC) carbon contents at the Institute of Geology and Mineralogy of the University of Cologne (Germany) using the Vario MICROcube (Elementar Corp.) and the DIMATOC 2000 (Dimatec Corp.) combustion analysers. Results are expressed in weight percentages relative to total amount of sample.

3.5. Grain-size analyses

A subset of 184 evenly spaced samples was selected for grain-size analysis, performed at the Institute of Geology and Mineralogy of the University of Cologne (Germany). For sample pre-treatment, 1.5 g of material was reacted with hydrogen peroxide (H_2O_2, 30%), hydrochloric acid (HCl, 10%), and sodium hydroxide (NaOH, 1M) in order to remove organic matter, the carbonate fraction and biogenic silica, respectively. Subsequently, the sample material was mixed with $Na_4P_2O_7$, mounted on a mechanical shaker for 12 h and treated for 1 min in an ultrasonic bath to enhance its dispersion. Sample aliquots were then measured with a Saturn DigiSizer 5200 laser particle analyser (Micromeritics Co., USA). Measurements were reiterated three times and individual results averaged.

3.6. XRF core scanning

Split core halves were analysed at the Institute of Geology and Mineralogy in Cologne (University of Cologne, Germany) using an Itrax XRF scanner (Cox Analytical Systems, Sweden). XRF scans were made using a Chromium tube set at 55 kV and 30 mA with a dwell time of 10 s and a step-size of 2.5 mm. Data are expressed in counts per second for incremental steps of 2.5 mm which are averaged at 1 cm intervals and then reduced to the subsampling interval (1 every 4th to every 8th cm).

3.7. $^{40}Ar/^{39}Ar$ geochronology

The set of $^{40}Ar/^{39}Ar$ dating of tephra layers described in Giaccio et al. (2017a) was augmented by additional dating of 4 tephra layers at the Berkeley Geochronology Center (BGC, Berkeley, USA) following the same procedures. Pristine sanidine and leucite crystals (where available) from TF-5, TF-10, TF-14 and TF-16 were separated by magnetic separation and heavy liquids, while adhering residues were removed via an ultrasonic bath of dilute (5–7%) hydrofluoric acid. All samples were finally handpicked to purity. Samples were co-irradiated with Alder Creek sanidine (ACs) crystals at Oregon State University (TRIGA reactor for 0.5 h and labelled irradiation 457PRA).

Ar isotopic measurements of sanidine and leucite crystals from Fucino samples (samples labelled TF) and ACs standards were analysed on a Noblesse 5-collector sector-magnet mass spectrometer, configured with one axial Faraday detector and four off-axis, symmetrically arrayed ETP ion counters. Quasi-uniform heating of each sample (a single grain of sanidine) was achieved via illumination with a CO_2 laser fitted with a beam-shaping lens to generate a flat energy profile of adjustable diameter, typically 2 mm at the target distance. Individual grains of ACs sanidine were heated for ~30 s at progressively increasing power levels (1.5–8 W, typically in 3–4 steps) until fusion was achieved. Evolved gas was exposed for several minutes to an approximately −130 °C cryotrap to remove H_2O, and to a GP-50 SAES getter to remove reactive gases. Integrated ages of the step-heating results of ACs were used to calculate J values and provide the basis for liner interpolation of J values for unknowns. J values of Fucino samples were determined by interpolation of a planar fit to J-values determined from the ACs fluence monitor (ACs monitor age = 1.1891 ± 0.0008 Ma, 1σ; Niespolo et al., 2017; Renne et al., 2011). Single grains of sanidine or leucite from Fucino samples were totally fused at 8–9 W. Five Ar isotopes were measured, with simultaneous measurement of ^{40}Ar, ^{37}Ar, and ^{36}Ar on separate ion counters over a period of ~800 s, alternating with peak hopping to position ^{38}Ar and ^{39}Ar on the same ion counter as ^{40}Ar. All signals were normalized to the ^{40}Ar ion counter. ^{36}Ar signal normalization was achieved through periodic measurement of the $^{40}Ar/^{36}Ar$ ratio of air (=298.56, Lee et al., 2006) inlet from an air-reservoir pipetting system. ^{37}Ar and ^{38}Ar signal normalizations were achieved through periodic measurement of ^{40}Ar from a static gas sample on relevant detectors in a round-robin peak-hopping procedure. Procedural blanks, matching sample gas extractions precisely but without firing the laser, were run every four analyses. The Noblesse instrument has sufficiently high resolution to distinguish an almost entirely hydrocarbon free shoulder at mass 36, where the measurement for ^{36}Ar is made. For further details of the analytical procedures refer to Deino et al. (2010). Interference corrections for all data are after Renne et al. (2015) and are included in the supplementary tables.

3.8. Tephra major element composition

In addition to the tephra recognised in F1-F3 in the previous study by Giaccio et al. (2017a), a careful revision of the core stratigraphy allowed us to recognise a new tephra layer (TF-5a at 24.97 m bbf). The major element composition of TF-5a was determined at IGAG-CNR (Rome, Italy) using a Cameca SX50 electron microprobe equipped with a five-wavelength dispersive spectrometer operating according to the instrumental settings

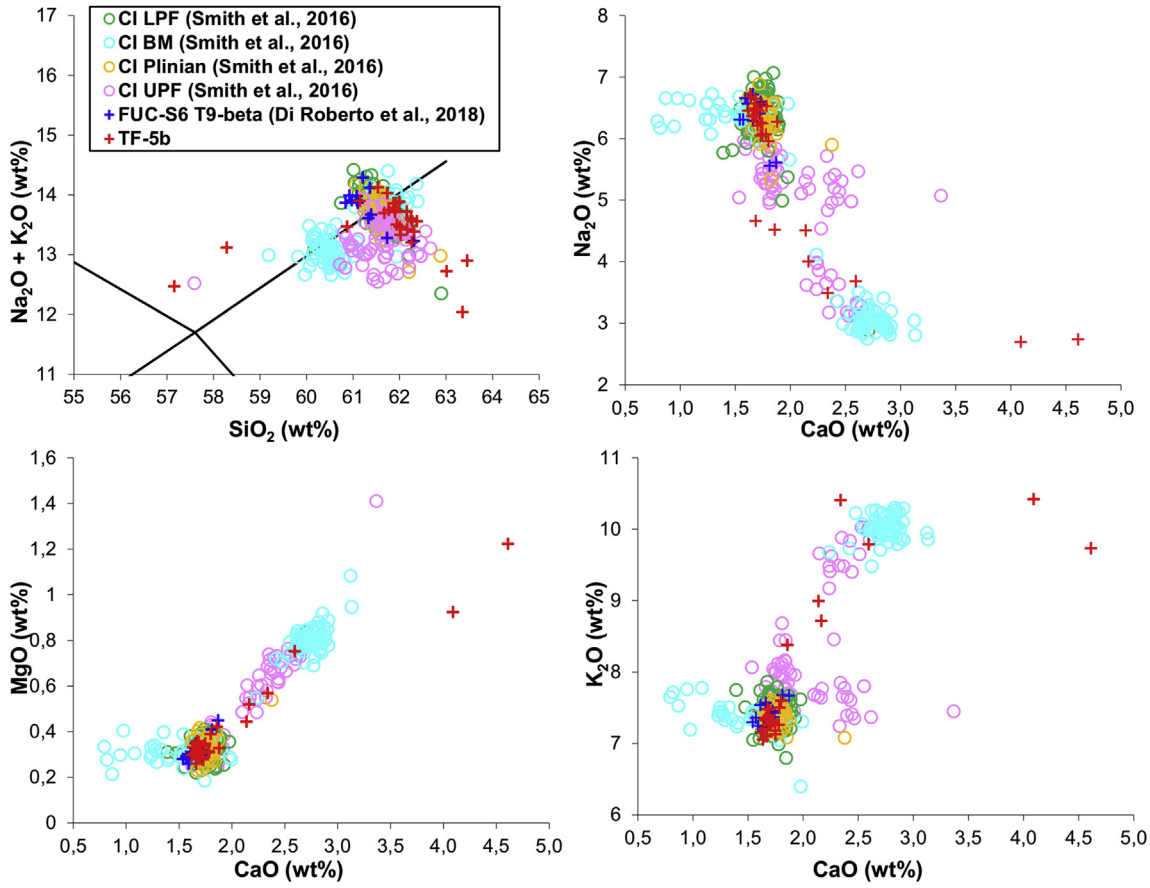

Fig. 2. Glass composition of TF-5a and correlatives - TF-5a glass composition is compared with that of T9-beta studied by Di Roberto et al. (2018) and that of Campanian Ignimbrite (CI) proximal deposits of the Lower Pumice Flow (LPF), the lithic-rich breccia (BM), the Plinian fallout (CI Plinian) and the Upper Pumice Flow (UPF) units after Smith et al. (2016). (For interpretation of the references to colour in this figure legend, the reader is referred to the Web version of this article.)

described in Giaccio et al. (2017a).

3.9. Age modelling

The age model and corresponding 95%-confidence interval were calculated with the Bacon software (Blaauw and Christen, 2011) written in the open-source statistical environment R (R Core Team, 2016). For comparison, calculations were also run with the BChron software (e.g., Parnell and Gehrels, 2015) which allows the input of multiple ages for a single dated layer. As Bacon only accepts a single age and corresponding uncertainty for each dated layer, a weighted mean age was calculated for chronologically consistent published and new radioisotopic ages. By doing so we introduced the assumption that errors are normally distributed around a single true value (i.e., a single probability peak in the density distribution of each dating) which is the main limit of this approach.

4. Results and discussion

4.1. Correlation of the TF-5a tephra

Tephra TF-5a (24.97 m bbf) is composed of relatively coarse (several mm) high vesicular pumices, blackish glass shards and sanidine and clinopyroxene crystals accompanied by abundant sedimentary and volcanic lithic fragments. Major element analyses of the newfound tephra TF-5a reveal a trachyte-phonolite composition with a SiO_2 content ranging between ~57 and ~63 wt % and clustering mainly between 61.5 and 62.5 wt %, an alkali sum of ~13–14 wt % (Fig. 2) and a variable alkali ratio (K_2O/Na_2O) of 1.0–3.8.

Based on these compositional features (Fig. 2), its stratigraphic order and the chronological constraints available for the F1-F3 succession, the TF-5a layer can be unambiguously correlated to the large Campanian Ignimbrite (CI) eruption, from Campi Flegrei. Specifically, the TF-5a layer is located between TF-5 and TF-7 which were correlated to Albano 5 and Y-7 tephra dated to ca. 39 ad 56 ka, respectively (Giaccio et al., 2017a). TF-5a shows a wide compositional spectrum, typical of the CI Upper Pyroclastic Flow (UPF; Fig. 2) with a rich assortment of crystals and lithic clasts (e.g., Rosi et al., 1996; Civetta et al., 1997). This relevant finding is confirmed by a recent discovery of the CI tephra in another core (FUC-S5-S6, Fig. 1b) retrieved from the Fucino Basin (Di Roberto et al., 2018). The CI tephra provides an additional precise and robust chronological anchoring point, as it is precisely dated at 39.8 ± 0.1 ka (Giaccio et al., 2017b) and is a widespread stratigraphic marker for Heinrich Event 4 (H-4; e.g., Giaccio et al., 2008; Zanchetta et al., 2017b).

4.2. $^{40}Ar/^{39}Ar$ geochronology

Detailed analytical results for each experiment are given in the supplementary material. Results are presented in Fig. 3 as inverse isochron diagrams (Deino and Potts, 1992). The weighted mean ages for combined intra- and inter-laboratory results are also presented as recommended ages for three tephra. Age uncertainties, as well as uncertainties in Ar isotopes, are here reported at 1σ.

TF-5 (23.70 m bbf) – Total fusion analyses of sanidine and

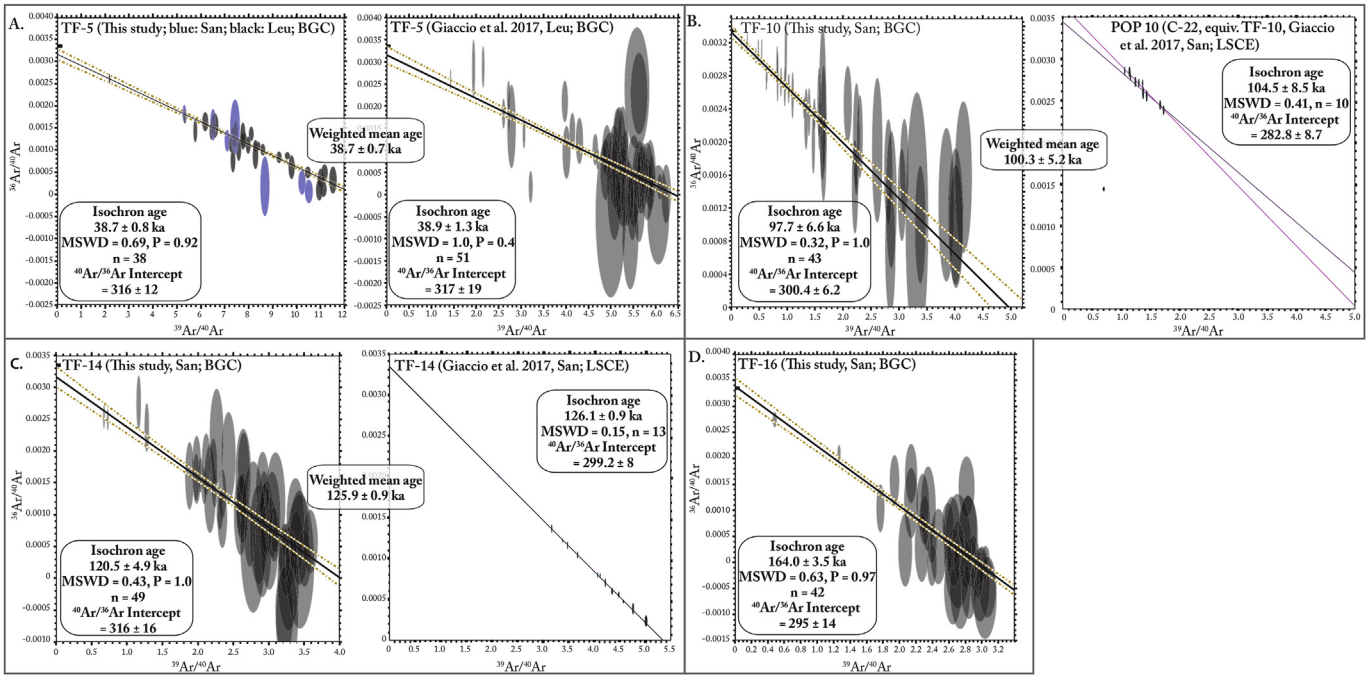

Fig. 3. Ar/Ar dating of Fucino tephra (TF) layers - Isochron ages of TF-5, TF-10, TF-14 and TF-16 determined at the Berkeley Geochronological Center (BGC) and at the Laboratoire des Sciences du Climat et de l'Environnement (LSCE) are combined together through a weighted mean approach. (For interpretation of the references to colour in this figure legend, the reader is referred to the Web version of this article.)

leucite produce two probability density function (PDF) ages (Fig. 3a). Treated as separate samples, outliers were removed from each population. The inverse isochron diagrams of these samples show that the leucite initial $^{40}Ar/^{36}Ar$ ratio is above the atmospheric value ($^{40}Ar/^{36}Ar_{leucite} = 319 \pm 13$) while the sanidine initial $^{40}Ar/^{36}Ar$ ratio overlaps with the atmospheric value ($^{40}Ar/^{36}Ar_{sanidine} = 310 \pm 30$) indicating that there is minor excess atmospheric Ar in the leucite but not in the sanidine population. This may explain why the leucite age is slightly younger than the sanidine age. Since the two ages are statistically indistinguishable at the 2σ level, we combine the analyses in a single PDF eliminating 3 more sanidine grains to yield a population with a mean square of weighted deviates (MSWD) nearest to 1. Putting the data all together in an isochron diagram, the inverse isochron intercept still indicates some excess atmospheric argon (316 ± 12), but not at 2σ. Nevertheless, to account for possible excess atmospheric argon, the isochron age is preferred over the PDF age. The combined isochron age for TF-5 is 38.7 ± 0.8 ka, MSWD = 0.69, P = 0.92, N = 38/43. The isochron age from Giaccio et al. (2017a,b), once recalibrated to the ACs fluence monitor age of 1.1891 Ma (Niespolo et al., 2017) and the decay constant of Renne et al. (2011), is of 38.9 ± 1.3 ka, MSWD = 1, P = 0.4, N = 51/53. The weighted mean age of the two isochrones is 38.7 ± 0.7 ka, which currently is the most representative age of the tephra.

TF-10 (41.10 m bbf) – This sample has a tight population with no outliers omitted. The isochron age indicates a $^{40}Ar/^{36}Ar$ intercept within uncertainty of atmospheric Ar (Lee et al., 2006), but for consistency with the other ages, the isochron age is preferred (97.7 ± 6.6 ka, MSWD = 0.32, P = 1, N = 43/43). Combining this result with the isochron age of Giaccio et al. (2012) for the POP1 tephra correlated with the C-22 eruption (Giaccio et al., 2012, 2017a,b), TF-10 yields a weighted mean isochron age of 100.3 ± 5.2 ka (Fig. 3b). These data were analysed at the Laboratoire des Sciences du Climat et de l'Environnement (CNRS-LSCE; Gif Sur Yvette, France). LSCE laboratory blank corrections are based on previous or bracketing blanks, with an uncertainty that reflects only the analytical precision of the prior or bracketing blank, rather than the long-term variability of blanks for the interval over which unknown analyses are performed in sequence (days to weeks). Unknowns analysed at BGC are corrected using another approach based on the long-term average value and its standard deviation measured in each blank analysis over days to weeks, which results in a larger uncertainty. Nevertheless, the interlaboratory comparisons continuously produce indistinguishable results, as is also the case for TF-14, (cf. Giaccio et al., 2017a). Thus the combined weighted mean age of 100.3 ± 5.2 ka is recommended as the most representative age of the tephra.

TF-14 (57.31 m bbf) – This sample produced a tight population of ages with no outliers. The inverse isochron diagram indicates that there might be some excess atmospheric Ar as seen in the elevated initial $^{40}Ar/^{36}Ar$ intercept (316 ± 16), so the isochron age is preferred. The isochron age for TF-14 is 120.5 ± 4.9 ka, MSWD = 0.43, P = 1, N = 49/49. For consistency, we combine this with the isochron age for TF-14 (126.1 ± 0.9 ka) published as a PDF age in Giaccio et al. (2017a,b) from LSCE results, yielding a weighted mean age of 125.9 ± 0.9 ka (Fig. 3c). This age is recommended as the most representative age of the tephra.

TF-16 (69.81 m bbf) – The inverse isochron diagram indicates an initial $^{40}Ar/^{36}Ar$ intercept within uncertainty of atmospheric argon, but for consistency, the isochron age is preferred. The isochron age for TF-16 is 164.0 ± 3.5 ka, MSWD = 0.63, P = 0.97, N = 42/42.

4.3. Age modelling

The proposed age model is based on the updated tephrostratigraphic framework discussed in Giaccio et al. (2017a) and considers the F1-F3 composite profile to be continuous, as no evidence for sedimentary hiatuses has been gathered so far. Calibrated ^{14}C ages for TF-1 and TF-3 correlative units (Smith et al., 2011) were converted from before 1950 to before year 2000 (b2k). New and

published radioisotopic $^{40}Ar/^{39}Ar$ ages for tephra layers were recalibrated using the new age of 1.1891 ± 0.0008 Ma for the Alder Creek Tuff sanidine (ACs) monitor standard proposed by Niespolo et al. (2017) and the ^{4}K total decay constant of Renne et al. (2011). We elaborate a homogeneous tephrochronological framework from 7.12 m to 75.39 m bbf, ranging in age between 9.2 ± 0.2 and 158.3 ± 1.5 (1σ) ka based on 15 $^{40}Ar/^{39}Ar$-dated and 2 ^{14}C dated tephra layers (see Table 1). The complete drainage of Lake Fucino in 1875 (125 y b2k) can be taken as a chronological constraint for the upper part of the sediment core. Owing to agricultural practices in the area, the uppermost part of the sediment succession underwent disturbance (ploughed horizon in the first 50 cm) and, presumably, soil loss. Thus, 1875 should be considered an "*ante quem terminus*". In order to chronologically constrain the deepest part of the composite (from 75.39 to 82.70 m bbf) we used the astronomical age of TF-21 correlative, which is the widespread regional tephra marker C-52 (Paterne et al., 2008). However, we doubled the reported uncertainty relative to the published data to account for possible unconstrained sources of error in the astronomically calibrated age uncertainty.

The resulting age-depth models produced by Bacon and BChron are statistically indistinguishable within 2σ confidence intervals (Fig. 4), but they display major difference in instantaneous sedimentation rates. By plotting instantaneous sedimentation rates against modelled age (Fig. 4) we observe that Bacon produces a relatively smoother curve. In contrast, BChron shows alternating phases of regular sediment deposition and short events of extremely slow deposition, probably because the input of multiple ages with small relative errors, and no room to accommodate differences in ages from the same horizon, may cause the algorithm to be forced to treat one or more co-occurring age results as outliers. Therefore, we choose to employ the Bacon age model for the current study, providing an age range from 0.13 ± 0.04 to 183.7 ± 8.6 (2σ) ka. The resulting temporal resolution for our multi-proxy time-series (XRF data and biogeochemical variables) varies from 30 to 300 years with a mean resolution of 90 years (median = 91 years; mode = 49 years). However, these values must be considered carefully as age uncertainties can vary largely (at 2σ level: min = 0.03 ka; max 4.5 ka; avg = 2.2 ka; mode = 0.5 ka) and some parts of the core composite suffer from a lack of dated points. This lack of dated points could possibly mask changes in sedimentation rates, especially during major environmental transitions. In the following text, if not otherwise specified, all uncertainties are expressed as 1σ.

4.4. Proxy significance

From the XRF scanner dataset we selected the Ti/Zr and Ca/Ti ratios for our palaeoenvironmental reconstruction, as these ratios can provide information on the detrital sediment input and on lake productivity, respectively.

Ti/Zr – Zr and Ti are both immobile elements that usually reside

Table 1
References: [a] this study; [b] Smith et al. (2011); [c] Galli et al. (2016); [d] Albert et al. (2013), [e] Giaccio et al., 2008, [f] Freda et al. (2006); [g] Giaccio et al. (2017a); [h] Giaccio et al. (2017b); [j] Giaccio et al. (2012); [k] Regattieri et al. (2015); [l] Iorio et al. (2014); [m] Laurenzi and Villa (1987); [n] Paterne et al. (2008). Note: all the $^{40}Ar/^{39}Ar$ ages are recalibrated using the new age of 1.1891 Ma for the ACs standard proposed by Niespolo et al. (2017).

#	Marker	Depth base (m)	Depth bbf base (m)	Correlative(s)	Age (ka ± σ)	Dating method	Weighted mean age (ka ± 1σ)	Modelled age (ka ± 1σ)
1	Drainage	0	0	–	0.13 ± 0.02	Historic event	0.125 ± 0.02	0.13 ± 0.02
2	TF-1	7.120	7.115	Sartania 1	9.6 ± 0.1[b]	^{14}C	9.4 ± 0.4 (artefact)	9.2 ± 0.5
				Pigna S. Nicola	9.3 ± 0.2[b]	^{14}C		
				San Martino	9.2 ± 0.1[b]	^{14}C		
3	TF-2	13.530	13.507	NYT	14.4 ± 0.2[c]	$^{40}Ar/^{39}Ar$	14.4 ± 0.2	14.5 ± 0.3
4	TF-3b	15.347	15.284	Ionian, not Y-1	18.0 ± 0.2[d]	^{14}C	18.0 ± 0.2	17.9 ± 0.3
5	TF-4	22.800	22.587	Albano 7	32.9 ± 2.0[e]	$^{40}Ar/^{39}Ar$	35.8 ± 0.6	36.0 ± 0.8
					36.8 ± 2.0[e]	$^{40}Ar/^{39}Ar$		
					35.7 ± 0.7[f]	$^{40}Ar/^{39}Ar$		
					44.8 ± 3.7[g]	$^{40}Ar/^{39}Ar$		
6	TF-5	24.030	23.697	Albano 5	38.7 ± 0.8[a]	$^{40}Ar/^{39}Ar$	38.8 ± 0.7	38.3 ± 0.5
					39.3 ± 1.0[g]	$^{40}Ar/^{39}Ar$		
7	TF-5a	25.300	24.967	C.I.	40.0 ± 0.1[h]	$^{40}Ar/^{39}Ar$	40.0 ± 0.1	40.0 ± 0.1
8	TF-6	27.420	27.054	Trefola quarry	n.a.	–	n.a.	54.8 ± 1.1
9	TF-7	27.770	27.314	Y-7	55.9 ± 0.5[g]	$^{40}Ar/^{39}Ar$	55.9 ± 0.5	55.7 ± 0.8
					55.0 ± 2.0[i]	$^{40}Ar/^{39}Ar$		
10	TF-8	32.490	32.101	Albano 3	68.3 ± 1.3[f]	$^{40}Ar/^{39}Ar$	70.0 ± 1.0	68.4 ± 1.0
					72.7 ± 1.7[e]	$^{40}Ar/^{39}Ar$		
11	TF-9	33.350	32.951	Albano 1	69.1 ± 0.9[f]	$^{40}Ar/^{39}Ar$	68.9 ± 0.6	69.4 ± 0.8
					68.6 ± 0.7[e]	$^{40}Ar/^{39}Ar$		
12	TF-10	41.520	41.101	C-22	92.1 ± 2.3[j]	$^{40}Ar/^{39}Ar$	100.3 ± 5.2	92.7 ± 3.5
					97.7 ± 6.6[a]	$^{40}Ar/^{39}Ar$		
13	TF-11	45.850	45.413	POP2a/TM24b	n.a.	–	n.a.	102.2 ± 2.1
14	TF-12	47.585	47.133	X-5	105.8 ± 1.5[j]	$^{40}Ar/^{39}Ar$	105.8 ± 1.5	106.021 ± 0.9
15	TF-13	49.105	48.621	X-6	109.1 ± 0.4[k]	$^{40}Ar/^{39}Ar$	109.1 ± 0.4	109.0 ± 0.6
					108.9 ± 0.9[l]	$^{40}Ar/^{39}Ar$		
16	TF-14	57.810	57.306	TM-36	126.0 ± 0.5[g]	$^{40}Ar/^{39}Ar$	126.0 ± 0.5	126.2 ± 1.3
					120.5 ± 4.9[a]	$^{40}Ar/^{39}Ar$		
17	TF-15	66.465	65.961	Vico C	153.5 ± 2.3[m]	$^{40}Ar/^{39}Ar$	153.5 ± 2.3	151.0 ± 2.5
18	TF-16	70.330	69.811	Vico B	159.6 ± 2.4[m]	$^{40}Ar/^{39}Ar$	160.6 ± 2.0	158.4 ± 2.5
					164.0 ± 3.5[a]			
19	TF-17	75.390	74.843	CF-V5	158.3 ± 1.5[g]	$^{40}Ar/^{39}Ar$	158.3 ± 1.5	164.7 ± 3.2
				OH-DP0624				
20	TF-18	80.005	79.445	Unknown	n.a.	–	n.a.	177.1 ± 4.2
21	TF-19	80.137	79.495	Unknown	n.a.	–	n.a.	177.2 ± 4.2
22	TF-20	82.110	81.443	Unknown	n.a.	–	n.a.	182.5 ± 4.2
23	TF-21	82.565	81.885	C-52	185.0 ± 2.5[n]	Orbital tuning	187.0 ± 4.0 (error increased)	183.7 ± 4.3
				C-52	189.0 ± 2.5[n]			

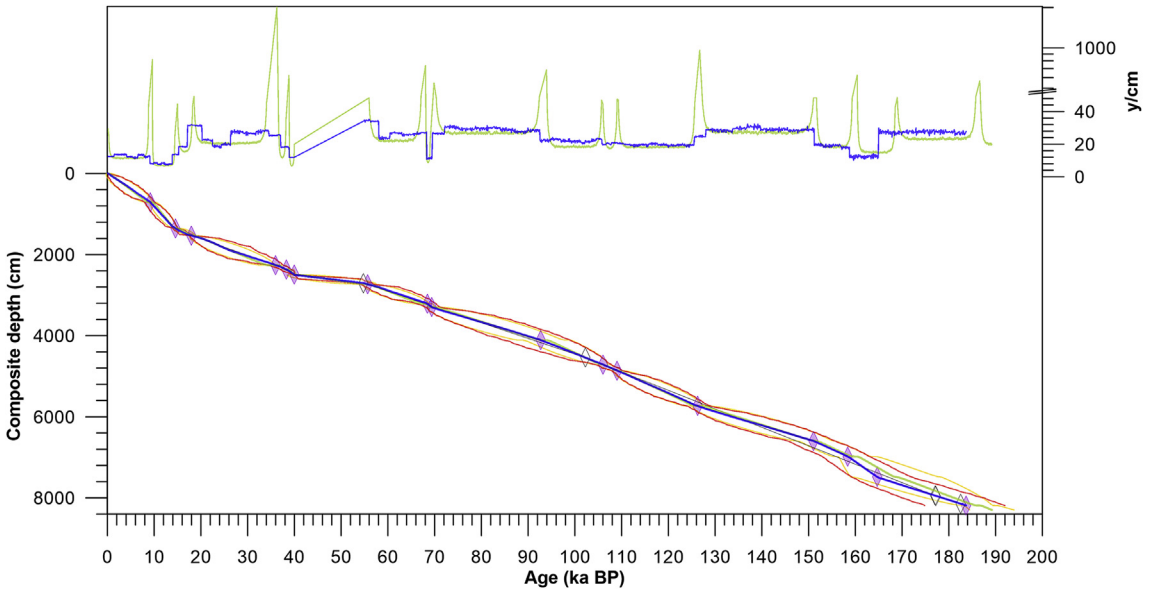

Fig. 4. Age model comparison - Comparison of selected Bacon (blue) and BChron (green) age models in terms of modelled mean age, 2σ confidence envelope (Bacon = red; BChron = yellow) and of accumulation rates plotted with the same colour key. Models are statistically indistinguishable at 2σ confidence level, nevertheless Bacon produces smoother curves. Note the break at 45 y/cm in the y-axis and the use of logarithmic scale thereafter. Diamonds indicate modelled tephra ages (Bacon) for tephra layers. (For interpretation of the references to colour in this figure legend, the reader is referred to the Web version of this article.)

in weathering resistant minerals (e.g., zircon, anatase, rutile, ilmenite). Nonetheless, Ti can also be incorporated in clay minerals. Thus, the Ti/Zr is generally used as a proxy for changes in grain size, with Ti being associated to clays and Zr to coarser silt and sand fractions (e.g., Kylander et al., 2011). Nevertheless, this geochemical-granulometric relationship is not a universal rule and has to be validated for Fucino Basin, where siliciclastic lithotypes rich in Ti and Zr-bearing minerals are nearly absent in the catchment (cf. Miccadei et al., 2012a,b). In such a context, the Ti/Zr might be indicative of different processes, including aeolian dust deposition and/or pyroclastic material.

Ca/Ti – In Fucino lacustrine sediments, Ca can be a product of *in situ* biologically mediated (endogenic) Ca-carbonate precipitation, to a minor extent of shell calcification in ostracodes, or of detrital influx from the large outcrops of marine limestones. Endogenic carbonates precipitate directly from the dissolved inorganic carbon pool of lake waters (DIC) mostly through algal fixation of CO_2 during photosynthesis (Freytet and Verrecchia, 2002). Therefore the process of bio-induced carbonate precipitation can be related to primary productivity and is largely influenced by hydrology, temperature and nutrient supply (e.g., Francke et al., 2016).

Differently from Ca, Ti is solely of detrital origin. Thus, the Ca/Ti ratio possibly expresses authigenic carbonate precipitation devoid of the detrital input.

TOC and TOC/TN – The concentration of total organic carbon (TOC) depends on the interplay of several processes, such as lake primary productivity, terrestrial input of organic matter, oxidation within the water column and post-sedimentation degradation processes (e.g., Meyers and Teranes, 2002).

The TOC/TN atomic ratio is commonly related to organic matter source (e.g., Meyers and Ishiwatari, 1993; Meyers and Lallier-Vergès, 1999) and generally reflects the proportion of aquatic vs. terrestrial plant contribution. Lower plants, such as aquatic phytoplankton and macrophytes, tend to concentrate N to a greater extent in respect to terrestrial plants. Therefore, organic matter derived solely from lacustrine production has C/N ratios typically <10, while organic matter derived from terrestrial plants usually has higher values (Meyers and Teranes, 2002).

Grain-size – Grain-size distribution can be used to trace variations in sediment transport processes. Nevertheless, the complex interaction of many factors operating from detritus generation to its transport and final deposition (e.g., Syvitski, 2007), together with the intrinsic complexity to mathematically model grain-size data (e.g., Beierle et al., 2002) make it difficult to produce a reliable model. Here we present a simplistic approach: by observing that classes finer than medium silt ($\varphi > 6$) show a strong positive inter-correlation and a strong negative correlation with classes coarser than medium silt ($\varphi < 5$), we define two end members, fine and coarse fractions. These two end members partially overlap in the medium-sized silt granulometric class. We interpret these two end members as the product of lower-energy (fine fraction) and higher-energy (coarse fraction) hydraulic processes, with variations most likely related to the position of coastal lines with respect to the drilling site or to wave energy and, thus, to lake level changes.

Calcite/quartz (Cal/Qtz) peak area – X-ray powder diffraction analyses on the lacustrine sediment succession show a common blend of minerals along the profile. The mineralogical assemblage mainly consists of calcite and quartz with minor amounts of mica series minerals. A wide range of accessory phases is also present, though this falls outside the scopes of this work. Here we evaluate the calcite/quartz peak area ratio as an additional proxy of the ratio between authigenic calcite precipitation within the lake and detrital influx from the catchment (e.g., Regattieri et al., 2017). Similarly, analyses of fluvial sediments show a large predominance of calcite over quartz (supplementary figure FS 2). This confirms that silicate rocks are a very marginal component in the Fucino Basin (cf. Miccadei et al., 2012a,b) and suggests that quartz is mainly of aeolian origin. Aeolian quartz grains are commonly found in maar lakes sediments from central Italy (Narcisi, 2000) and, in higher abundance, in loess deposits along the Apennine chain (Giraudi et al., 2013) and in central Italy (Boretto et al., 2017).

4.5. Bivariate statistics

Although tectonic activity and sediment redeposition can not be excluded at the F1-F3 site, we have no observation for such

processes. Therefore, we focus our study on palaeoenvironmental changes and try to define some specific processes by means of a simple statistical analysis of selected proxies.

We test the Ti/Zr ratio as a proxy for grain-size variations by comparing it against the fine fraction and against sediment sorting (*sensu* Folk and Ward, 1968) (Fig. 5). We find that it is not possible to define a single robust relationship between variations in sedimentary parameters and the Ti/Zr ratio. Furthermore, we do not observe any strong correlation with the other proxies, as scatter plots results in a cloud of dispersed points. Thus we suggest the Ti/Zr ratio might be influenced by processes external to the catchment acting as a source of detrital material. In particular, we propose a relationship between higher (lower) values in the Ti/Zr ratio and increased (reduced) influx of material depleted in heavy mineral from outside the catchment. To this regard, the Ti/Zr scatter plot of lacustrine sediments *sensu stricto* and of tephra layers (Fig. 5) shows that volcanic ashes from proximal and distal sources constitute a primary source of Ti and Zr-bearing minerals. We find that it is not possible to define a mixing process between detrital material of local origin and volcanoclastic material, as eruptive products do not have a peculiar signature in Ti/Zr. In fact, even single eruptive products can cover the entire spectrum of sediment Ti/Zr variability. Therefore, the Ti/Zr ratio is probably more related to clastic input, either of primary or secondary aeolian origin, where for secondary origin we refer to aeolian dust possibly funnelled into the lake by the catchment drainage system.

We observe a strong positive correlation ($R = 0.96$) between the Ca/Ti log ratio and TIC, with points clustering in a narrow interval in the TIC Log(Ca/Ti) scatter plot (Fig. 6). This could suggest a minor influence of detrital limestone on the Ca-carbonate pool and that Log(Ca/Ti) and TIC can be primarily considered as proxies for endogenic Ca-carbonate precipitation. Only for extreme compositions (i.e., $\text{Log(Ca/Ti)} > 3$) we observe a change in strength of this relationship. This is consistent with observations made from Boyle (2000), where extreme compositional characteristics of the sediments, such as particularly elevated Ca concentrations, can hinder

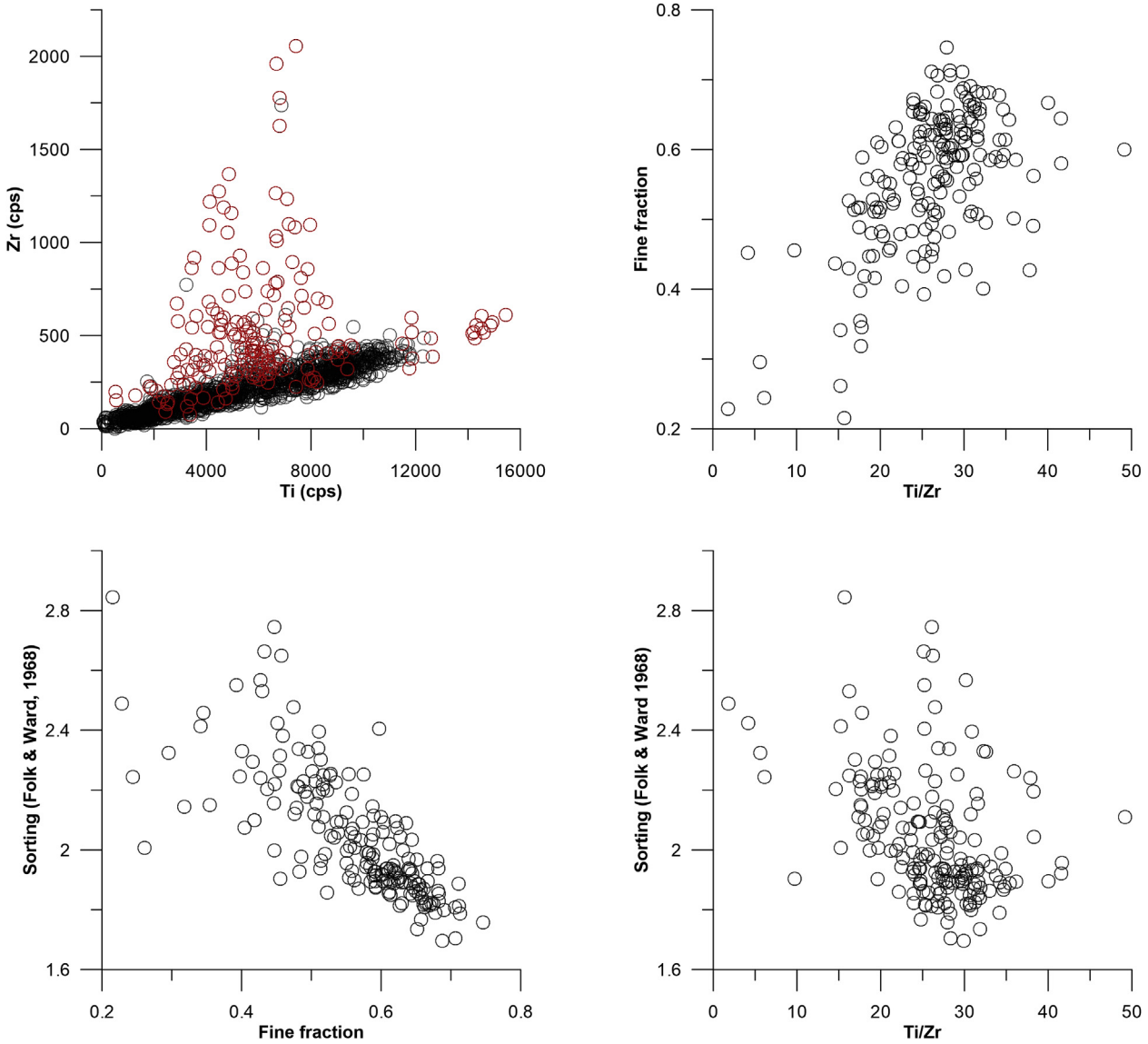

Fig. 5. Sediment sources identification - Scatterplots clarifying relationships between: (upper sinistral) volcanoclastic input of Ti, Zr-bearing material (red) and lacustrine detrital fraction (black); (upper dextral) fine fraction and Ti/Zr ratio in the lacustrine sediments; (lower sinistral) sediment sorting and fine fraction in the lacustrine sediments; (lower dextral), sediment sorting and Ti/Zr ratio in the lacustrine sediments. (For interpretation of the references to colour in this figure legend, the reader is referred to the Web version of this article.)

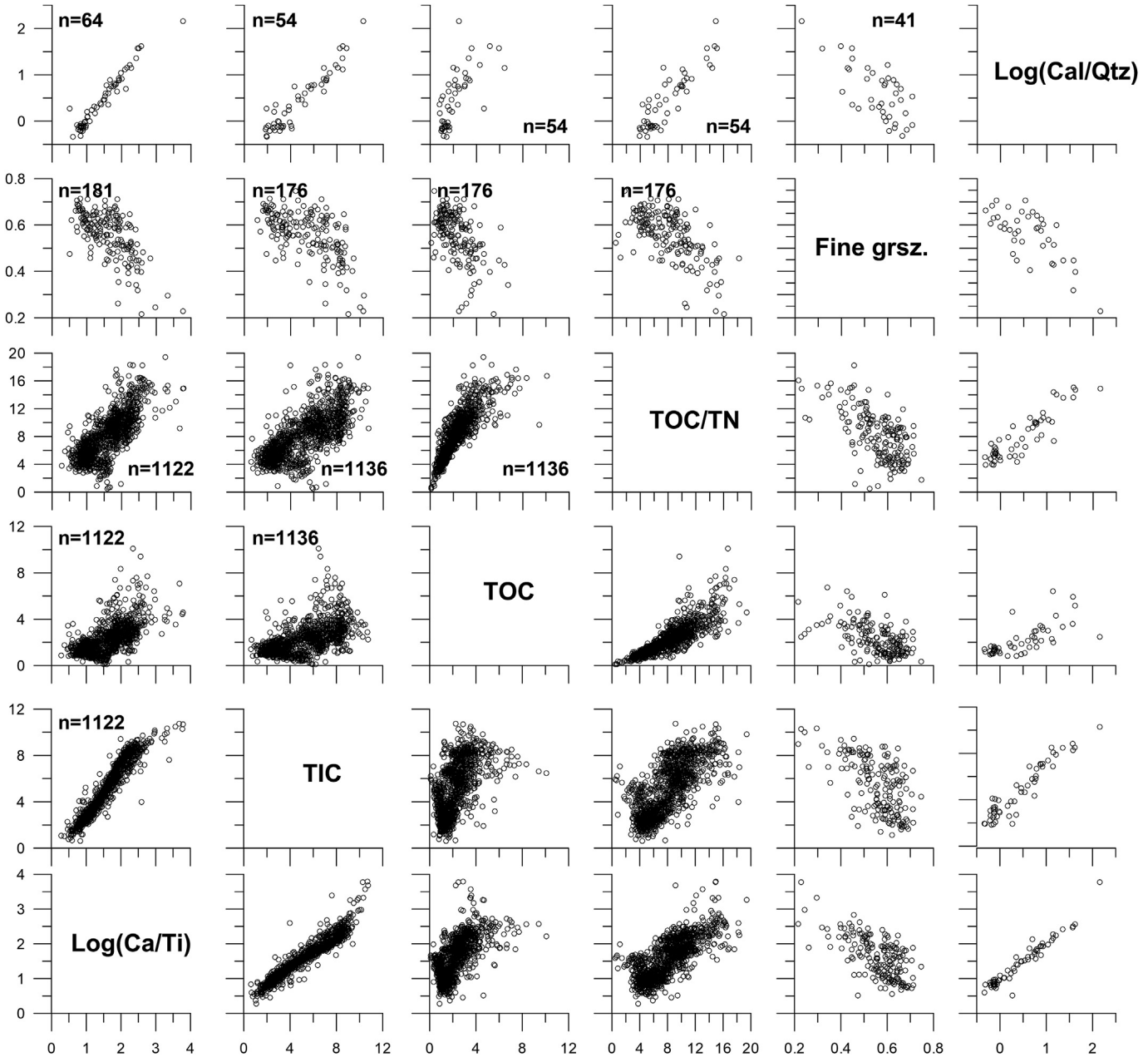

Fig. 6. Proxy bivariate diagrams - Scatterplots for different biogeochemical, mineralogical and particle size variables. The magnitude of statistical populations (n) is reported as well.

the correct determination of Ti.

Although TOC has strong correlation coefficients with other geochemical variables (R ranges from |0.53| to |0.81|, Table 2), data points are widely dispersed in the scatter plots and do not trace any robust linear correlation (Fig. 5). Points cluster in a narrow interval only in the TOC/TN vs TOC scatter plot, indicating a relationship between higher content in organic matter and increased supply from the terrestrial component. TOC/TN also shows strong positive correlation values with Log(Ca/Ti) and TIC, while it is negatively correlated with the fine fraction. Scatter plots show that these relationships hold only on a broad scale, as points tend to disperse around a common trend (Fig. 5). This testifies to the development of a wide array of environmental settings, where an increased (decreased) contribution of terrestrial organic matter is in general mirrored by enhanced (reduced) lake primary productivity in a shallower, strongly evaporated (deeper, freshwater) lake.

The fine fraction shows a weak negative correlation with TIC and the Log(Ca/Ti) ratio suggesting a general relationship between shallow (deep) lacustrine facies and increased (reduced) importance of endogenic carbonate precipitation. By observing this trend together with the anti-correlation between fine fraction and TOC/

Table 2
Pearson correlation values for selected proxies.

R Pearson	Log(Ca/Ti)	TIC	TOC	TOC/N	Fine	Log(Cal/Qtz)
Log(Cal/Qtz)	0.97	0.94	0.71	0.90	−0.64	1
Fine	−0.65	−0.59	−0.54	−0.61	1	−0.64
TOC/N	0.75	0.71	0.81	1	−0.61	0.90
TOC	0.61	0.54	1	0.81	−0.54	0.71
TIC	0.96	1	0.54	0.71	−0.59	0.94
Log(Ca/Ti)	1	0.96	0.61	0.75	−0.65	0.97

TN, we suggest that the development of a shallow lake with alkaline, nutrient rich waters under strong evaporation regimes could boost primary productivity.

4.6. Proxy time-series overview

The investigated Fucino sedimentary successions record the local environmental evolution during the last two glacial to interglacial cycles (i.e., Saalian to Eemian and Weichselian to Holocene; Fig. 7). Analysis of proxy time series enables us to discern two different environmental end members which can be related to the local climatic expression of glacial and interglacial conditions. During the Weichselian and Saalian glaciations Lake Fucino was characterised by the deposition of fine-grained sediments with low

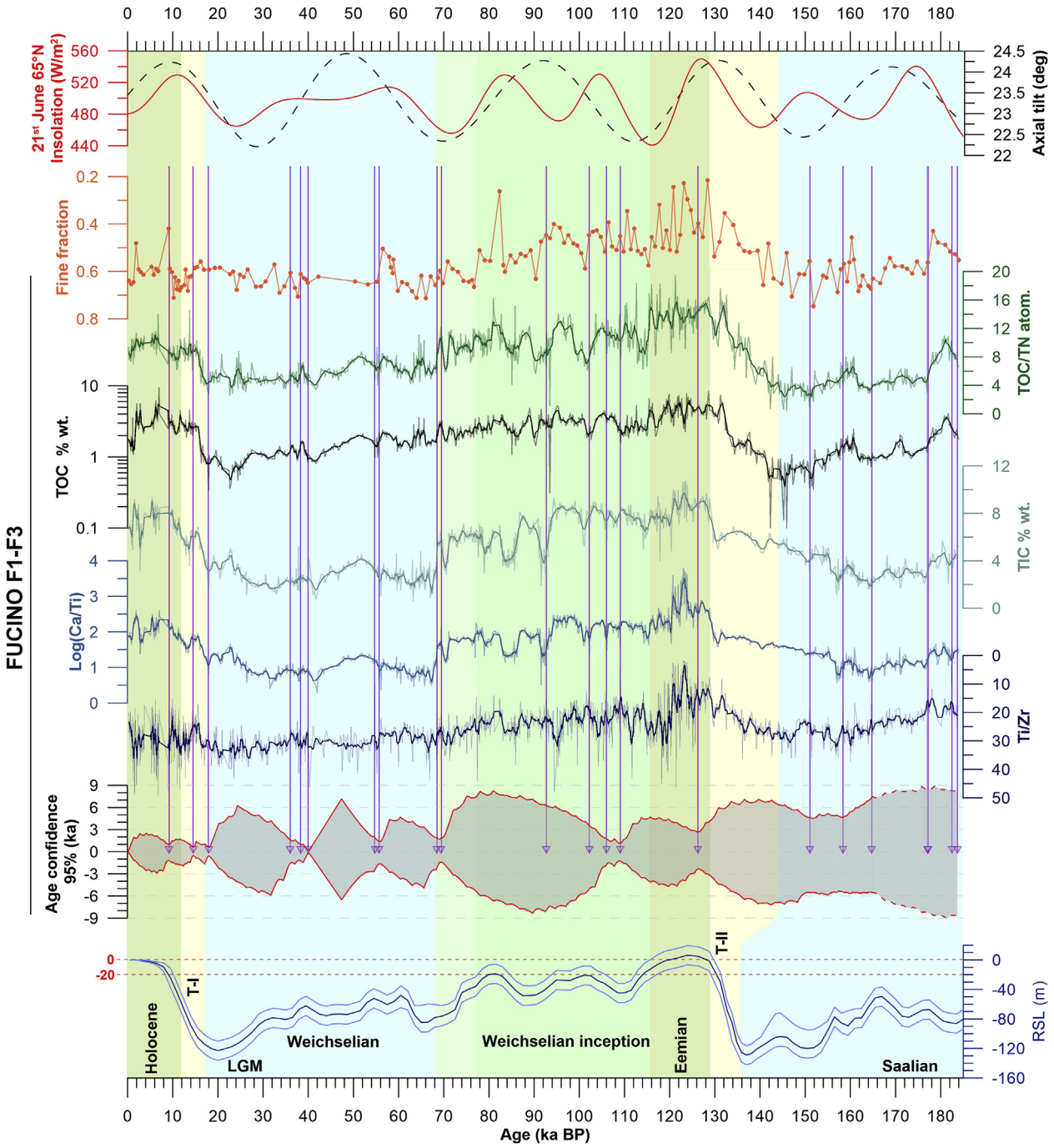

Fig. 7. Time-series overview - Fucino F1-F3 proxy time series plotted together with calculations for past Earth's axial tilt and 65°N summer solstice insolation (Laskar et al., 2004) and global Relative Sea Level (RSL) variations (Waelbroeck et al., 2002) as indicative of global ice volume. The two dotted red lines indicate the present day sea level and the −20 m threshold, as an indicator of little Northern Hemisphere (NH) ice volumes outside Greenland under interglacial conditions (PAGES, 2016). Glacial and interglacial stages are named after the traditional European continental climatic stratigraphy. The Last Glacial Maximum (LGM) is reported as well. Fucino F1-F3 time series, excepts for grain size, are smoothed with a 7 points running average. Purple triangles and vertical lines indicate the position of tephra layers according to their modelled age. At the bottom 2σ age uncertainties; dashed red lines from ca. 164 to ca. 184 ka indicate chronology relying on the orbitally tuned age of tephra TF-21/C-52. (For interpretation of the references to colour in this figure legend, the reader is referred to the Web version of this article.)

content of organic matter, mainly of lacustrine origin. Endogenic calcite precipitation is low compared to the local detrital input (Fig. 7). These proxies indicate a relatively large and deep lake, surrounded by a barren environment. To this regard, the high mountain ranges that border Fucino Basin display considerable quantities of glacial and periglacial sediments (e.g., Giraudi and Frezzotti, 1997; Giraudi et al., 2011a; Giraudi, 2012) with relict moraines down to an altitude of ca. 1000 m a.s.l. Glacial deposits may have represented the source of clastic material transported by streams and wind currents down into the lake. Studying late Pleistocene glacial dynamics and lake level oscillations, Giraudi and Frezzotti (1997) proposed an in-phase relationship between glacial advances (retreats) and lake level rise (drop). High lake level during glacial/stadial is probably related to increased meltwater input and/or reduced evaporation during warmer months. In this view, meltwater may have sustained the local hydrogeological budget during glacial periods, commonly characterised by a drier climate (e.g., Follieri et al., 1989; Brauer et al., 2007).

On the contrary, during the Holocene, the early Saalian and, in particular, during the Eemian Lake Fucino was characterised by the deposition of coarser sediments with higher content of organic matter with more prominent terrestrial signature. Furthermore, detrital clastic input was reduced (Ti/Zr) and endogenic calcite precipitation dominated (Fig. 7). All the proxies indicate a shallower lake and a catchment with enhanced soil stability, probably related to vegetation development.

According to our independent chronology we observe that the onset of interglacial conditions in the Fucino Basin has been a protracted process. In particular, our proxy time-series (Ti/Zr, TOC, Log(Ca/Ti) and TOC/TN ratios) suggest that the local transition from the Saalian glaciation to the Eemian interglacial was a slow and progressive process accomplished only at 129 ± 2 ka and was possibly characterised by a sharp acceleration during its late stages (Fig. 7). The lack of dated points in this interval does not allow us to precisely date the beginning of the local Saalian-Eemian transition, however we observe similar protracted environmental changes during the local Weichselian-Holocene transition. Our data indicate that the transition to the current interglacial possibly lasted more than 10 ka starting at around 26 ± 3 ka, after the local glacial maximum was reached (cf. Giraudi, 2017). Furthermore, it is important to notice that different proxies show different trends both on a long-term scale and on a shorter scale (Fig. 7). This suggests the development of a wide spectrum of environmental responses at both lake and catchment scale across glacial-to-interglacial transitions. In this sense, the transition from glacial to interglacial conditions at the catchment scale is basically different from the definition of a termination based, for instance, on marine deposits (T-II in Fig. 7 represented by sea-level from Waelbroeck et al., 2002).

The Eemian appears pervaded by millennial-scale environmental changes, with the response of different proxies not always occurring in phase (Fig. 7). For instance, the final demise of Eemian interglacial conditions is diachronous depending on which proxy is used to define the transition. Similarly, we observe substantial diachroneity in the onset of Weichselian full glacial conditions, with a decline of TOC/TN, TIC, Log(Ca/Ti) and Log(Cal/Qtz) at around 68.5 ± 0.9 ka, while the other proxies suggest an earlier demise. The Weichselian and the Saalian glacial periods seem to exhibit a subdued oscillation of proxies in comparison with the Eemian interglacial and the Eemian-Weichselian transition phase (Fig. 7). This is not a unique feature of our record, indeed Mediterranean palaeoclimate records show the greatest amplitude of millennial scale variations during phases of intermediate ice volume (e.g., Tzedakis, 2005). In Fucino Basin this can also be related to the proximity of glaciated areas dampening environmental responses to climate changes. Therefore, the complexity of the climatic history and of environmental responses of different proxies at Fucino calls for a cautionary approach in tracing correlations between different archives, especially when age models rely on assumptions and age uncertainties can not be unambiguously stated. Moreover, it also suggests that during glacial to interglacial transitions a simple definition of "termination" may not fully capture the complex interplay of environmental processes in terrestrial environments (e.g., Wilson et al., 2015).

4.7. Regional climatic correlations

4.7.1. Selected regional records for comparison

For a comparison of the Fucino F1-F3 multi-proxy record with other records we selected those which provide an independent chronology or can be easily synchronised via tephrostratigraphic correlations (Fig. 1a).

The Lake Monticchio pollen record, spanning over the last 135 ka (Brauer et al., 2007 and references therein), displays 10 common tephra layers with Fucino. We select "mesic woody taxa", "Mediterranean taxa" and "steppic taxa" pollen percentages to be correlated with our record. Dominance of mesic woody taxa indicates absence of marked seasonal moisture shortage, while periods of intermediate abundance indicate moderate seasonal moisture deficiency. Mediterranean taxa include sclerophyllous trees and shrubs tolerant of summer drought, but intolerant of cold winter conditions. Steppic taxa are tolerant of cold events and arid conditions (Brauer et al., 2007). Although not shown in figures, we also considered the pollen archive from Tenaghi Philippon peatland (e.g., Müller et al., 2011; Milner et al., 2016), Greece, that contains two MIS 5 tephra layers in common with our record (i.e., X-6/TF-13 and C-22/TF-10) and the Campanian Ignimbrite (Wulf et al., 2018).

Five tephra layers allow us to stratigraphically correlate Fucino and Ohrid records over the last 160 ka. Two additional tephra layers allow synchronisation of Ohrid and Monticchio lake records at ca. 29 and 9 ka. From the Lake Ohrid record we use K-countings as a proxy of clastic terrigenous input and TOC as a proxy for lake productivity and for organic matter preservation in the surface sediments (Francke et al., 2016).

We also select some speleothem records from the Mediterranean region and from Southern Europe due to their of robust U-Th chronologies (e.g., Dorale et al., 2004) which ensure a high degree of confidence for the proposed correlations with the Fucino record.

The oxygen stable isotope composition of speleothems ($\delta^{18}O_{speleo.}$) from the Apuan Alps (Northern Apennines, Fig. 1a) is considered to be largely controlled by variations in rainfall amount in response to North Atlantic Ocean sea surface temperature (SST) variations and represents a powerful tool to reconstruct the hydrological balance of this region (e.g., Drysdale et al., 2005, 2007; 2009; Regattieri et al., 2014). Similarly, the $\delta^{18}O$ record from the neighbouring Sulmona lacustrine succession also provides a detailed archive of the hydrological change over the Apennines for the 130–90 ka interval (Regattieri et al., 2015, 2017). Furthermore, this record can be firmly synchronised with F1-F3 via four common tephra layers (Fig. 8).

The $\delta^{18}O_{speleo.}$ values from Soreq cave (Israel, Fig. 1a) are tightly connected with Eastern Mediterranean Sea surface conditions. Here, changes in sea surface water composition, arising from the balance of precipitation, terrestrial freshwater supply and evaporation, are recorded in speleothems. Thus, minima (maxima) in $\delta^{18}O_{speleo.}$ correspond to more positive (negative) water hydrological balance over this region (Bar-Matthews et al., 2000).

The $\delta^{18}O_{speleo.}$ from Villars Cave (France; Fig. 1a) is a mixed proxy for local temperature and hydrology and thus is closely mirrored by variations in $\delta^{13}C$, which is directly linked to local vegetation

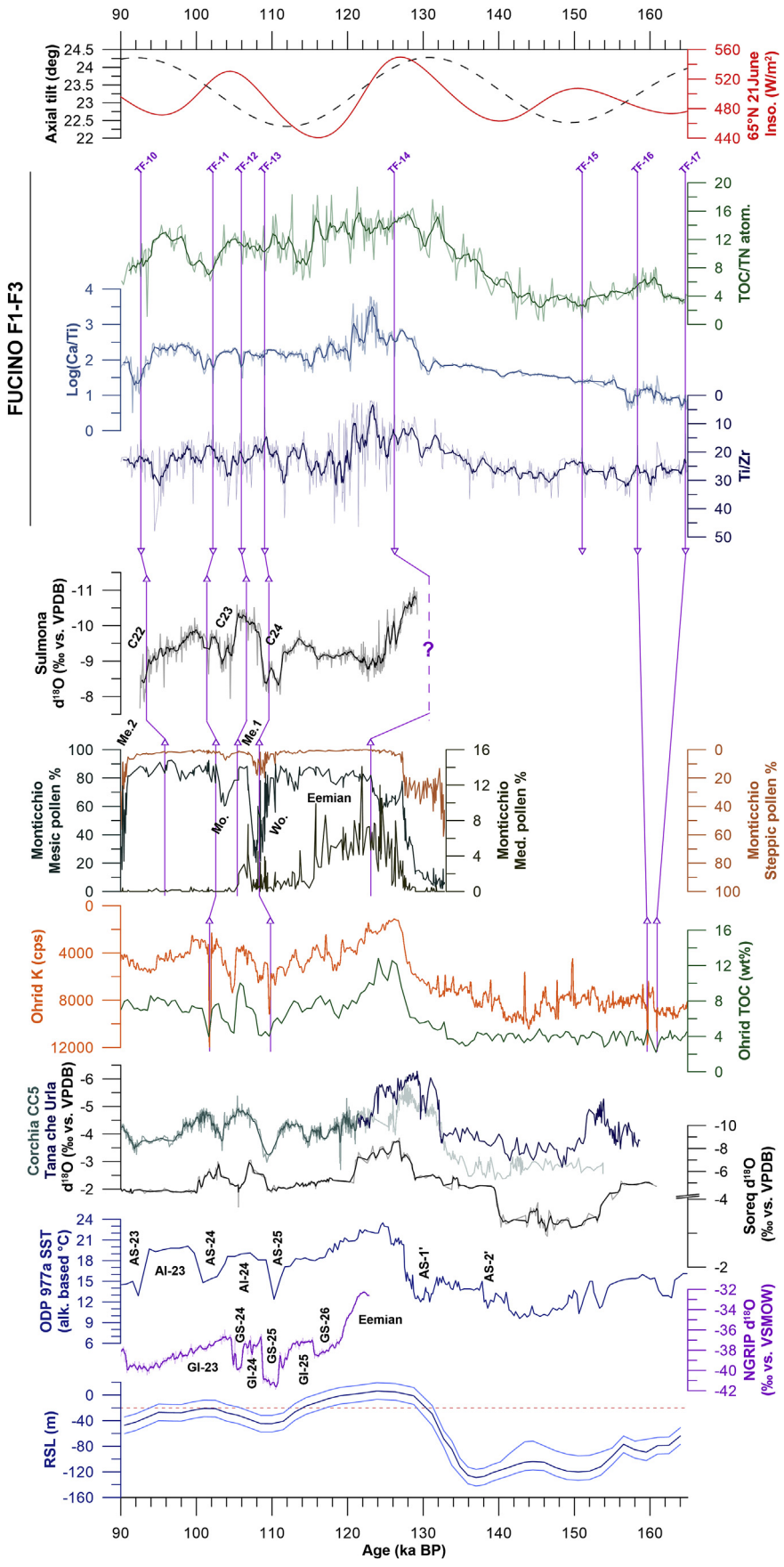
FUCINO F1-F3
Axial tilt (deg)
65°N 21 June Inso. (W/m²)
TF-10
TF-11
TF-12
TF-13
TF-14
TF-15
TF-16
TF-17
TOC/TN atom.
Log(Ca/Ti)
Ti/Zr
Sulmona d¹⁸O (‰ vs. VPDB)
C22
C23
C24
?
Me.2
Me.1
Mo.
Wo.
Eemian
Monticchio Mesic pollen %
Monticchio Med. pollen %
Monticchio Steppic pollen %
Ohrid K (cps)
Ohrid TOC (wt%)
Corchia CC5 Tana che Urla d¹⁸O (‰ vs. VPDB)
Soreq d¹⁸O (‰ vs. VPDB)
ODP 977a SST (alk. based °C)
AS-23
AI-23
AS-24
AI-24
AS-25
AS-1'
AS-2'
GS-24
GS-25
GS-26
GI-23
GI-24
GI-25
Eemian
NGRIP d¹⁸O (‰ vs. VSMOW)
RSL (m)
Age (ka BP)

coverage. Thus minima (maxima) indicate warmer (colder) conditions in the North correlated with an increase (decrease) in precipitation and, ultimately, with vegetation expansion (contraction) (Genty et al., 2003, 2010).

Comparison with proxy data from marine sites ODP 977a (Martrat et al., 2004; Alboran Sea; Fig. 1a) and MD95-2043 (Fletcher et al., 2010; Alboran Sea; Fig. 1a) enables us to evaluate the propagation of past climate changes in the Mediterranean region from the North Atlantic. Here we use Alkenone based SST reconstruction from core ODP 977a (Martrat et al., 2004) and palynological data from core MD95-2043. Regarding the MD95-2043 pollen record we adopt the two pollen-based indexes proposed by Fletcher et al. (2010). The first index, $\mathbf{I_t}$, is defined as $Q_e/(CC + Q_e)$, where Q_e is the number of pollen grains of *Quercus* evergreen type and CC is the combined number of pollen grains of *Cedrus* and *Cupressaceae*. The second index, $\mathbf{I_p}$, is defined as $Q_d/(SD + Q_d)$, where Q_d is the number of pollen grains of *Quercus* deciduous type and SD is the number of pollen grains of semi-desert taxa (*Artemisia*, *Chenopodiaceae* and *Ephedra distachya* type). Low (high) values in these indexes reflect cooler (warmer) and dryer (more humid) conditions, respectively.

We also report the $\delta^{18}O$ record of Northern Greenland ice cap (NGRIP, NGRIP members, 2004), which is considered a proxy for local temperature.

All the records are discussed in consecutive time slices corresponding to periods of large, intermediate and minimum global ice volume (Figs. 7 and 9–10) as expressed by the global relative sea level (RSL, Waelbroeck et al., 2002) curve. To this regard, Tzedakis (2005) proposed a correlation between the environmental response of terrestrial ecosystems in the Mediterranean region to climatic forcing and continental ice sheet volume and configuration, as ice sheet configuration strongly affects atmospheric circulation patterns (e.g., Pollard and Barron, 2003). In this sense, the transition from glacial to interglacial conditions at the catchment scale is basically different from the definition of termination based on marine deposits. Important differences at the sub-orbital scale can exist between the evolution of the Fucino hydrological proxies and global reference curves such as that representing sea level changes.

4.7.2. Saalian glaciation (large ice volume)

As the chronology of the oldest part of our record (i.e., below TF-17) relies solely on the astronomically tuned age of TF-21 correlative, the tephra C-52 (Paterne et al., 2008), we focus on the main aspects of this period. Between ca. 184–165 ka, the F1-F3 record shows a progressive transition from intermediate glacial-interglacial conditions towards markedly glacial conditions over the Apennines. In general, decreasing terrestrial organic matter supply is coupled with increasing detrital input into the lake, suggesting progressive vegetation decline and increasing erosion in the lake catchment. Furthermore, the increased fine-grained fraction suggests the establishment of a lower hydraulic energy regime, which can be explained by an increase in lake level. Higher lake levels in Lake Fucino are likely related to increased melt-water supply from incipient snow/ice fields in the catchment. A local glacial advance during this period is also supported by studies of Giraudi and Giaccio (2015) in the nearby Mount Velino.

Beginning shortly after the deposition of TF-17 (modelled age 164.7 ± 3.2 ka), we observe a steady increase of lake primary productivity (Fig. 8) which might correspond to the beginning of a 30 ka-long lasting warming. This trend is also reflected by a gradual decrease in detrital inflow likely sustained by the reappraisal of terrestrial vegetation and pedogenesis. Compared to the increase in lake primary productivity, this phase of enhanced soil stability has a shorter duration, and ends around the time of deposition of TF-16 (modelled age 158.4 ± 2.5 ka). Between the deposition of TF-16 and ca. 145 ka lake primary productivity is elevated and increases over time, the lake level shows periodical large fluctuations, whereas the catchment is characterised by a barren environment favouring erosion (Fig. 8). This environmental setting could be explained by the local maximum in summer insolation and by a different seasonal response of lake primary productivity (summer) and of glaciated mountain areas (winter snow accumulation and summer ablation). At around ca. 145 ka we observe a phase of progressive catchment stabilisation marking the beginning of the transition to interglacial conditions (Fig. 8). The K record of Lake Ohrid testifies to a similar evolution, even though with a slight chronological offset, i.e. a reduction in clastic supply between 154 and 145 ka followed by a short phase of stadial conditions between ca. 145–140 ka (Fig. 8). Differently from lacustrine archives, marine core ODP 997a and the Soreq Cave speleothem record indicate prolonged stadial conditions (minima in SST and $\delta^{18}O_{speleo.}$) with a cold and dry climate dominating until ca. 140 ka (Fig. 8).

4.7.3. Termination II (T II)

After ca. 145 ka all the proxies in our record suggest an almost synchronous trend towards interglacial conditions: we observe progressive sediment coarsening, coupled with reduced detrital input, increased influx of terrestrial organic matter and increased lake productivity (Fig. 8). The other records also indicate progressively warmer and more humid climate promoting early soil formation and vegetation expansion. However, this warming trend shows some major interruptions. The Fucino record, similar to the records from Soreq cave and, to a lesser extent, Lake Ohrid, shows a cold and arid event at ca. 133 ka (Fig. 8). At around 134.0 ± 3.4 ka we observe a steep increase in Fucino TOC, TOC/TN and Ti/Zr coupled with a reduction in the fine fraction suggesting a rapid transition to interglacial conditions. However this is not mirrored by endogenic carbonate precipitation, which remains low (Fig. 8). This could be explained by a more intense water renewal in Fucino Lake under an enhanced hydrological regime as observed in speleothems from the northern Apennines (Fig. 8; Regattieri et al., 2014; Drysdale et al., 2004, 2007, 2009 and cf. Regattieri et al., 2016). These data, together with the palynological information from the onset of the Lake Monticchio record, indicate that enhanced rainfall and warm temperatures favoured forest expansion possibly all over the central Mediterranean area (cf. Sadori et al., 2016; Sinopoli et al., 2018; Milner et al., 2016) at the end of the Saalian glacial period.

4.7.4. Eemian interglacial (minimum ice volume)

In Fucino the Eemian interglacial can be divided in two periods. The first period lasts from 128.6 ± 2.1 to 119.5 ± 2.2 ka and is characterised by the highest primary productivity, the shallowest lake level and by minimum clastic input. We interpret the first part of the Eemian as the local expression of the Last Interglacial (LIG)

Fig. 8. Record comparison – Time-slice 1, from the Saalian to the early Weichselian. Note that each record is plotted against its own chronology and common tephra markers are traced from one record to the other. Fucino F1-F3: Purple lines and labels identify Fucino F1-F3 tephra layers (TF) and their correlatives in other records. Sulmona Basin: Cold-arid (C) events 22 to 24 as identified by Regattieri et al. (2015). Lake Monticchio: Note plotting on different percentage scales, in particular steppic taxa are plotted on a reverse scale. Main palynological events recognised by Brauer et al. (2007): Woiliard (Wo.), Mointagu (Mo.) and Melisey (Me.) 1 and 2. Core ODP 977a: Alboran Sea stadials (AS) and interstadials (AI) after Martrat et al. (2004). NGRIP record: Greenland stadials (GS) and interstadials (GI) after Rasmussen et al. (2014). RSL: the red dotted line indicates the −20 m sea-level threshold, corresponding to little Northern Hemisphere (NH) ice volumes outside Greenland under interglacial conditions (PAGES, 2016). (For interpretation of the references to colour in this figure legend, the reader is referred to the Web version of this article.)

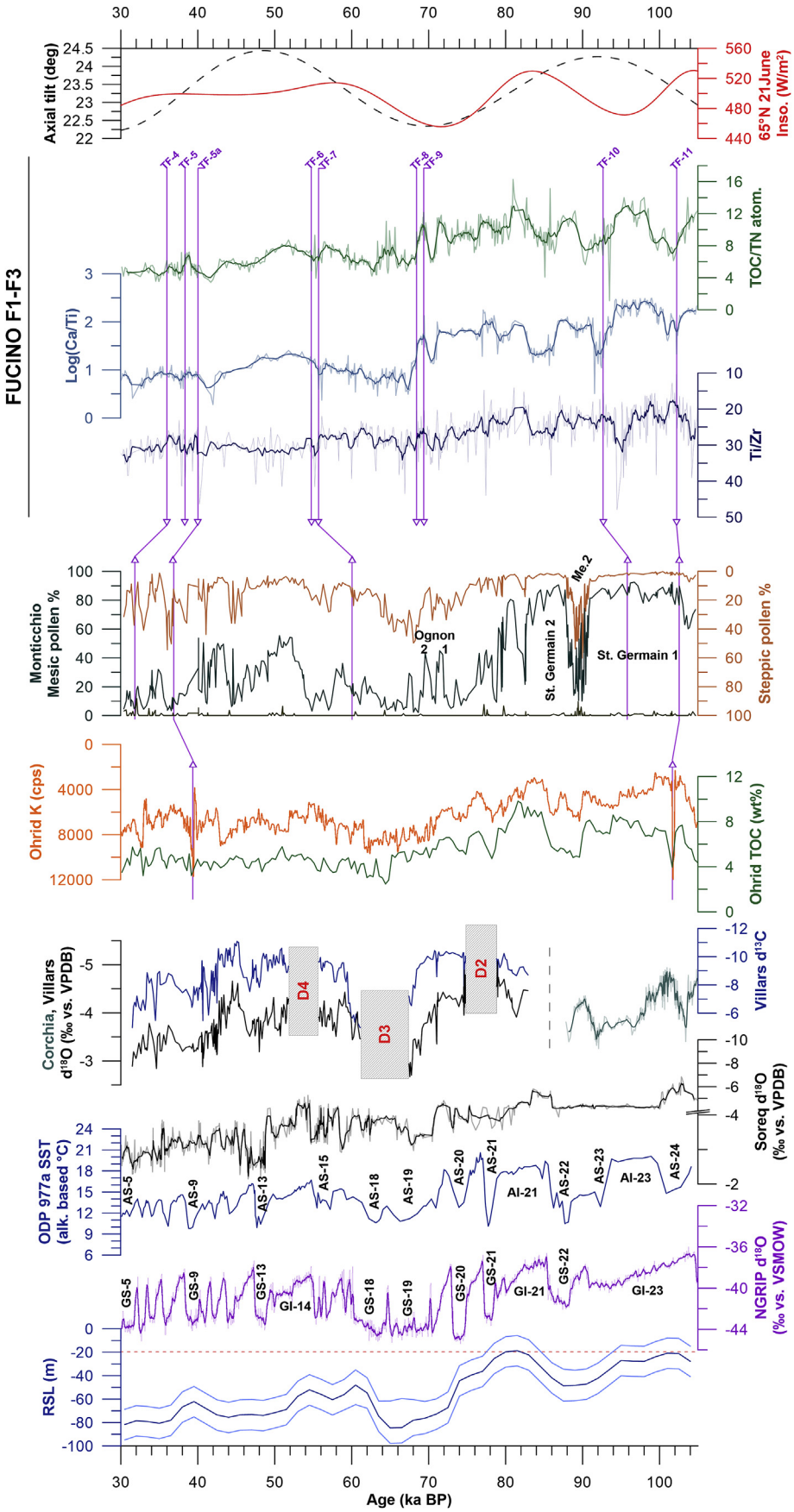
FUCINO F1-F3
Axial tilt (deg)
65°N 21June Inso. (W/m²)
TF-4
TF-5
TF-5a
TF-6
TF-7
TF-8
TF-9
TF-10
TF-11
Log(Ca/Ti)
TOC/TN atom.
Ti/Zr
Monticchio Mesic pollen %
Steppic pollen %
Ognon 2
Ognon 1
St. Germain 2
Me-2
St. Germain 1
Ohrid K (cps)
Ohrid TOC (wt%)
Corchia, Villars d18O (‰ vs. VPDB)
D4
D3
D2
Villars d13C
Soreq d18O (‰ vs. VPDB)
ODP 977a SST (alk. based °C)
AS-5
AS-9
AS-13
AS-15
AS-18
AS-19
AS-20
AS-21
AI-21
AS-22
AS-23
AI-23
AS-24
NGRIP d18O (‰ vs. VSMOW)
GS-5
GS-9
GS-13
GI-14
GS-18
GS-19
GS-20
GS-21
GI-21
GS-22
GI-23
RSL (m)
Age (ka BP)

maximum. The subsequent phase, lasting from 119.5 ± 2.2 to 115 ± 2.3 ka, is characterised by lower primary productivity and clastic input (Fig. 8) and corresponds to the late Eemian, a transitional phase to the Weichselian glacial inception. The LIG maximum is associated with a strong millennial scale variability with three maxima from 128.6 ± 2.1 to 124.3 ± 1.5 ka (encapsulating TF-14), from 123.7 ± 1.6 to 121.4 ± 1.9 ka and from 121.1 ± 1.9 to 119.5 ± 2.2 ka (Fig. 8). These peaks in Log(Ca/Ti), TIC, TOC and TOC/TN correspond to maxima in coarse grain size and possibly indicate shallower lake levels in response to progressively increasing Northern Hemisphere (NH) summer insolation. They are separated by periods of finer sediment deposition, suggesting a contrasting hydrological regime with an alternation of drier and wetter periods during the LIG maximum. Similarly, the Lake Monticchio pollen record shows a maximum extent of Mediterranean taxa, testifying to increased summer aridity (note that the original Monticchio varve age of 123.0 ± 7.8 ka for TF-14 correlative, the TM-36 tephra, although consistent with the radiometric dating of 125.9 ± 0.9 ka, constrains the Eemian chronology to younger ages in the Monticchio record). Mediterranean taxa also depict rapid and large oscillations confirming that brief phases of increased summer drought alternated with more humid phases. For this time span, speleothem records from the Apuan Alps (e.g., Regattieri et al., 2014) and the isotopic record from the Sulmona Basin (Regattieri et al., 2017), located near the Fucino Basin, indicate a progressive reduction in the hydrological balance with a subdued high frequency oscillation (Fig. 8). Similarly, Lake Ohrid shows a progressive reduction in soil stability (Fig. 8) associated with phases of rapid forest contraction and expansion (cf. Sinopoli et al., 2018). The transition to the final part of the Eemian was characterised by colder and drier climatic conditions as, for instance, expressed by a reduction in SSTs at ODP 977a (Fig. 8) and by the interruption of flowstone growth at Tana che Urla cave at 120.3 ± 1.0 ka (modelled age by Regattieri et al., 2014). The timing of this transition is consistent with the progressive decline in Earth's axial tilt and in precession index, suggesting a strong orbital control for the onset and the demise of the LIG maximum in our record.

During the late Eemian, our record shows three other peaks in TOC and TOC/TN centred at around 119.3 ± 2.1, 117.2 ± 2.3 and 115.6 ± 2.3 ka, respectively (Fig. 8). These peaks can be compared to those of the LIG maximum for their intensity, however they occur in a different environmental context. In contrast with the LIG maximum, the late Eemian is characterised by reduced lake primary productivity and by increased detrital inflow into the lake (Fig. 8). Coherently, records from Monticchio and Ohrid lakes indicate progressive vegetation reorganization (reduction in Mediterranean taxa) accompanied by a partial soil loss (Fig. 8). These processes can be correlated with a swift decline in precipitation and with a progressive cooling; this is indicated by the palaeohydrological records from the Sulmona Basin (Regattieri et al., 2015, 2017), by speleothems from the Apuan Alps (Drysdale et al., 2007) as well as from Israel (Bar-Matthews et al., 2000) and by Alboran Sea SSTs (Martrat et al., 2004), respectively (Fig. 8).

4.7.5. Weichselian glacial inception (intermediate ice volume)

At 115.0 ± 2.3 ka we observe profound changes in the environmental configuration that initiated the final demise of the Eemian interglacial and the beginning of the Weichselian glacial inception. Our record indicates an initial transition towards a deeper lake with fewer nutrients and increased detrital input (Fig. 8). At 113.0 ± 2.1 ka, this trend is replaced by a progressive lake level shallowing superposed with rapid fluctuations in grain-size lasting until 105.0 ± 1.0 ka. During this period, TF-13 and TF-12 allow us to synchronise our record with Sulmona, Monticchio and Ohrid lake records (Fig. 8).

The TF-13 is a correlative of the X-6 tephra, a well-known stratigraphic marker for the cold event C-24 (e.g., Regattieri et al., 2015; Zanchetta et al., 2016; Wulf et al., 2018) corresponding to Greenland Stadial (GS) 25. During the C-24 Sulmona, Corchia and Soreq records show a 2–3 ka phase of reduced precipitation (Fig. 8) and pollen records of Lake Monticchio (Brauer et al., 2007), Tenaghi Philippon (Wulf et al., 2018) and Ohrid Lake (Sinopoli et al., 2018) show a profound decline of mesic taxa (corresponding to “Melisey I” stadial conditions) in close stratigraphic relation to the deposition of the X-6 tephra layer. The K record from Lake Ohrid, in agreement with spikes in Ti/Zr at Fucino, indicates enhanced soil erosion at the time. TF-12, which is a correlative of the widespread X-5 tephra (Giaccio et al., 2017a), marks the re-initiation of warm and wet conditions over the Mediterranean Region as testified by the deepening of Lake Fucino and by the increase of mesic woody taxa at Monticchio (Fig. 8). This is also testified by the Sulmona lacustrine record and in speleothems from Corchia and Soreq caves (Fig. 8). Regattieri et al. (2015) demonstrated that this event, corresponding to Greenland Interstadial (GI) 24, is coeval with the deposition of sapropel S4 in the central Mediterranean Sea and to the first interval of S4 deposition in the Eastern Mediterranean Sea, which corresponds to the precession minimum/NH summer insolation maximum at 105 ka.

Between 104.7 ± 1.1 ka and 102.1 ± 1.7 ka, Lake Fucino indicates a persistent shallower lake level coupled with increased detrital input. At that time Monticchio (Brauer et al., 2007) and Ohrid (Sinopoli et al., 2018) pollen records show a shift towards stadial conditions (the so-called “Montaigu event”). This event can be traced also in speleothems across the Mediterranean area (Bar-Matthews et al., 2000; Drysdale et al., 2007, Fig. 8).

Tephra layers TF-11 and TF-10 allow the synchronisation of Fucino with Sulmona, Monticchio and Ohrid lake records between ca. 105 and 98 ka. These two tephra layers bracket the onset and demise of a humid and warm phase, favouring forest recovery (the so-called “St. Germain I” event) and soil development (Figs. 8 and 9). The small increase in Fucino primary productivity and the gentle cooling trend in Greenland throughout GI-23 associated with a SSTs resumption suggest a moderate NH warming at the time. After ca. 94 ka, the investigated records indicate a general shift towards stadial conditions. At Fucino we observe the progressive development of a deep and large lake with a lower trophic state (Fig. 9). The tephrostratigraphic correlation with Monticchio and Tenaghi Philippon (TF-10) suggests a prolonged phase (ca. 5 ka) of forest expansion at the time, then followed by a rapid contraction of mesic taxa and the first advance of steppic taxa (the so-called “Melisey 2” event; Fig. 9). This can be correlated with the speleothem growth interruption in the Apuan Alps at ca. 87.8 ka (Drysdale et al., 2005, 2009, Fig. 9, CC5 stalagmite) and the onset of stadial GS-22 in Greenland (Rasmussen et al., 2014). At Sulmona, the

Fig. 9. Record comparison – Time-slice 2, early to late Weichselian. Note that each record is plotted against its own chronology and common tephra markers are traced from one record to the other. Fucino F1-F3: Purple lines and labels identify Fucino F1-F3 tephra layers (TF) and their correlatives in other records. Lake Monticchio: Note plotting on different percentage scales, in particular steppic taxa are plotted on a reverse scale. Main palynological events recognised by Brauer et al. (2007): Melisey (Me.) 2. Villars Cave: stalagmite growth hyatuses (D) 2 to 4 after Genty et al. (2010). Core ODP 977a: Alboran Sea stadials (AS) and interstadials (AI) after Martrat et al. (2004). NGRIP record: Greenland stadials (GS) and interstadials (GI) after Rasmussen et al. (2014). RSL: the red dotted line indicates the −20 m sea-level threshold, corresponding to little Northern Hemisphere (NH) ice volumes outside Greenland under interglacial conditions (PAGES, 2016). (For interpretation of the references to colour in this figure legend, the reader is referred to the Web version of this article.)

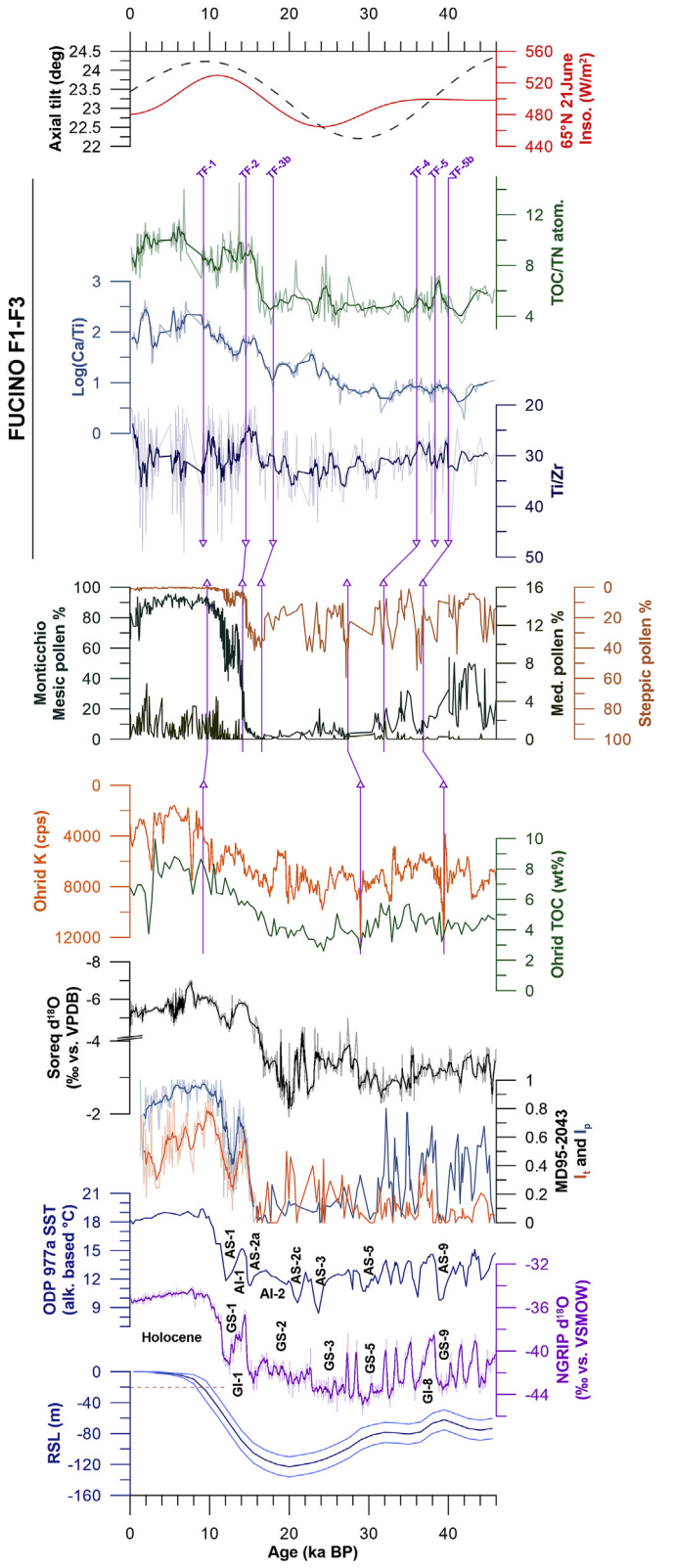

Fig. 10. Record comparison – Time-slice 3, from the late Weichselian to the Holocene. Note that each record is plotted against its own chronology and common tephra markers are traced from one record to the other. Fucino F1-F3: Purple lines and labels identify Fucino F1-F3 tephra layers (TF) and their correlatives in other records. Lake Monticchio: Note plotting on different percentage scales, in particular steppic taxa are plotted on a reverse scale. Core ODP 977a: Alboran Sea stadials (AS) and interstadials (AI) after Martrat et al. (2004). NGRIP record: Greenland stadials (GS) and interstadials (GI) after Rasmussen et al. (2014). RSL: the red dotted line indicates the −20 m sea-level threshold, corresponding to little Northern Hemisphere (NH) ice volumes outside Greenland under interglacial conditions (PAGES, 2016). (For interpretation of the references to colour in this figure legend, the reader is referred to the Web version of this article.)

correlative tephra of TF-10 (POP1/C22 modelled age 93.4 ± 2.2 ka in Regattieri et al., 2015 and 92.7 ± 3.5 ka here) marks the end of lacustrine sedimentation and the definitive establishment of a fluvial system (Giaccio et al., 2012; Regattieri et al., 2015).

The following climatic period is not well constrained chronologically either at Fucino, nor at Lake Ohrid because of the absence of radioisotopically dated tephrostratigraphic markers and it is not recorded by the Apuan Alps speleothems as they had already ceased to grow probably because of the development of glacial conditions in the catchment area (Drysdale et al., 2007; Isola et al., 2019). The general indication from the different records (Fig. 9) is of moderate warming favouring the resumption of forested areas ("St. Germain II" as recorded at Monticchio). Sinopoli et al. (2018) suggested that "St. Germain II" was characterised by initial wet conditions followed by progressively increasing moisture shortage. This hypothesis is also confirmed by speleothems from Soreq Cave, that indicate the reappraisal of wetter conditions from ca. 86 to 82 ka followed by a rapid decline in precipitation amount. This rapid decline in precipitation is recorded in Fucino as a sharp lake level shallowing at 82.4 ± 4.0 ka. The timing of this climatic phase is in perfect agreement with the onset, acme and decline of GI-21 (Rasmussen et al., 2014, Fig. 9).

For the period until ca. 73 ka Fucino indicates the progressive development of a large and deep lake with reduced primary productivity and increased detrital input. These are coupled with a progressively reduced, yet largely fluctuating, TOC/TN. Similarly, Monticchio shows a drastic drop in mesic woody taxa at ca. 80 ka, followed by the progressive expansion of steppic areas (Fig. 9). In the Mediterranean region this climatic phase marks an important vegetation reorganization setting the end of major forest expansions under relatively stable and prolonged interstadial conditions (Martin-Puertas et al., 2014). This period is coupled with profound soil erosion at Lake Ohrid as shown by the K record (Francke et al., 2016, Fig. 9). Rapid oscillations in SSTs (AS-21, AI-20, AS-20; Martrat et al., 2004) and in $\delta^{18}O$ values at Soreq cave (Bar-Matthews et al., 2000), indicate the onset of colder and less humid conditions. Particularly intense cooling from ca. 78.8 to 75.5 ka is also indicated by the D2 growth hiatus in Villars cave (Genty et al., 2003, 2010, Fig. 9). This is in good chronological concordance with the onset of GS-21 under declining NH summer insolation (Fig. 9).

Between 73 ka and the deposition of TF-8 (modelled age 68.4 ± 1.0 ka), our record suggests a partial resumption of vegetation in the catchment and lake primary productivity. This is consistent with the short lived "Ognon I" and "Ognon II" events as they appear in the Lake Monticchio pollen record (Brauer et al., 2007) and with an SST increase during AI 20 and 19 (Martrat et al., 2004; cf. Sánchez Goñi et al., 2013, Fig. 9). In particular, we suggest the peak in TOC/TN bracketed in between TF-9 and TF-8 is can be correlated with the "Ognon II" stadial, with these two tephra layers marking its acme and decline phases, respectively.

4.7.6. *Weichselian glaciation (large ice volume)*

In concomitance with the deposition of TF-8 (modelled age 68.4 ± 1.0 ka) we observe a rapid decline in lake primary productivity which is coeval with the establishment of Weichselian full glacial conditions (MIS 4) over the central Apennines (Fig. 9). We correlate this transition to the phase of mountain glacier advance on the Apennines (Giraudi and Giaccio, 2015), rapid expansion of steppic areas observed at Lake Monticchio (Brauer et al., 2007) and of swift SST reduction during AS-19 and AS-18 (Martrat et al., 2004,

Fig. 9). Following the published scheme of climatostratigraphic correlations, we correlate this phase to Heinrich Event H-6 (Martrat et al., 2004) and to the Villars growth hiatus D3 (Genty et al., 2003, 2010) and, ultimately, to GS-18 (Rasmussen et al., 2014, Fig. 9). After H-6 we observe an incipient lake level shallowing associated with increased primary productivity and reduced detrital input at Lake Fucino. These observations are consistent with forest expansion and soil development as recorded in Monticchio (Brauer et al., 2007, Fig. 9) and Ohrid lakes (cf. Sadori et al., 2016). We correlate this period to warming during early AI-17/GI-17 (Fig. 9, cf. Martrat et al., 2004).

Subsequently, Fucino TOC, TOC/TN and grain size analyses suggest the establishment of a phase (from 58.9 ± 2.2 to 56.5 ± 0.9 ka) characterised by a shallower lake level possibly related to decreased effective precipitation. This is consistent with the reappraisal of warmer climatic conditions as testified by increased mesic woody taxa at Lake Monticchio, reduction in soil erosion at Lake Ohrid and an increase of SSTs during AI 17 and 16 (Fig. 9, cf. Martrat et al., 2004). In Villars Cave a new phase of speleothems growth begins at ca. 61 ka. The isotopic signals of Villars Cave speleothems, together with that of Soreq Cave speleothems, suggests the establishment of a more vigorous yet unstable hydrological regime. At 55.9 ± 1.0 ka speleothem growth in Villars Cave ceases (hiatus D4), probably in response to cave flooding (Genty et al., 2003, 2010). This might correspond to a stronger pluviometric regime as suggested by the reappraisal of a deep lacustrine/low hydraulic energy facies at Fucino shortly before the deposition of TF-7 (modelled age 55.7 ± 0.8 ka) and by Soreq speleothems (more negative $\delta^{18}O$ values synchronous with the deposition of sapropel S2 – Bar-Matthews et al., 2000, Fig. 9).

After the deposition of the tephra couplet TF-7 and TF-6 (modelled ages 55.7 ± 0.8 and 54.8 ± 1.1 ka, respectively) we observe a particularly low sedimentation rate in our record. This may be a general indication for drier climatic conditions in the time span between TF-6 and TF-5a (CI tephra, modelled age 40.0 ± 0.1 ka). Indeed, our multi-proxy record indicates a progressive reduction of lake primary productivity and a contraction of catchment vegetation (Fig. 9). In the other records this transition from interstadial to stadial conditions is superposed with a rapid alternation of cooling and warming events (Fig. 9, cf. Martrat et al., 2004: AI-14 to AS-9, and Rasmussen et al., 2014: GI-14 to GS 9). This climatic phase then culminates into the extremely cold and dry Heinrich Event 4 (H4; e.g., Fedele et al., 2003) which is stratigraphically marked by the Campanian Ignimbrite tephra (e.g., Giaccio et al., 2008, 2017b). This event is not particularly evident in our record, probably because at the time the local environment was already barren and lake primary productivity was nearly at its minimum until 28.0 ± 1.7 ka (Figs. 9 and 10). Between ca 40 and 28 ka large millennial-scale oscillations in grain-size and Ti/Zr in our record seem to correlate with rapid variations in steppic taxa at Lake Monticchio, events of increased soil instability at Ohrid and periods of enhanced rainfall as recorded by the MD95-2043 pollen record (Fig. 9, $\mathbf{I_p}$). These rapid alternations of warming and cooling events are also testified by the ODP 977a SST and Greenland temperature records (Fig. 9, cf. Martrat et al., 2004: AI-8 to AS-5 and Rasmussen et al., 2014: GI-8 to GI-5).

At 26.0 ± 1.9 ka, Fucino indicates progressively increasing primary productivity coupled with a steadier hydrological regime and with progressively less intense detrital input (Fig. 9). Similarly, K-intensities of the Lake Ohrid record indicate renewed soil stability starting at around 24 ka. This can be correlated with a contraction of steppic areas, as shown by reduced abundance of steppic taxa at Lake Monticchio under warmer conditions as testified by increasing SST at ODP site 977a and by the $\mathbf{I_t}$ pollen index from MD95-2043 (Fig. 9).

4.7.7. Termination I and the Holocene (small ice volume)

After 20.0 ± 1.9 and ka we observe an initial resumption of stadial conditions culminating shortly after the deposition of TF-3b (modelled age 17.9 ± 0.3 ka). At lakes Fucino and Ohrid the resumption of stadial conditions is testified by a reduction in primary productivity and by increased detrital influx, while at Lake Monticchio it is expressed by expansion of steppic taxa (Fig. 9). This can be associated with a shallower Fucino lake level in a context of a regional colder and drier climate (indicated by ODP 977a SST and by MD95-2043 pollen indexes; Figs. 7 and 10) during the Oldest Dryas stadial (cf. Giraudi, 1996). After the deposition of TF-3b we observe a short phase of moderate increase in lake primary productivity coupled with high detrital input that we interpret as the beginning of the local glacial retreat dated by Giraudi (2017) at ca. 17–18 ka. At ca. 16.7 ± 0.4 ka, shortly before the deposition of TF-2 (modelled age 14.5 ± 0.3 ka), we observe a steep increase in lake primary productivity coupled with a reduction in detrital input (Fig. 9). The TF-2 corresponds to the Neapolitan Yellow Tuff which is a regional marker for the late Bølling-Allerød warming (e.g., Magny et al., 2006). This allows us to synchronise our record with Monticchio and to evaluate the phase of forest expansion during the Late Glacial. This synchronisation suggests a lag of ca. 2.5–3 ka in temperate forest expansion relative to the beginning of environmental changes as they are expressed in our record. After the deposition of TF-2, lake primary productivity proxies indicate two brief interruptions in the trend towards Holocene interstadial conditions, approximately from 14.0 ± 0.6 to 11.6 ± 0.8 and from ca. 11.0 to 10.5 ka, when climate conditions were colder and possibly dryer and when the lake level was lower (cf. Giraudi, 1996; Giraudi and Mussi, 1999, Fig. 9). Considering the low chronological control for this interval, we can only speculate that these oscillations may be related to Younger Dryas and pre-Boreal oscillations (e.g., Magny et al., 2006). The upper part of our record is incomplete, and does not add any relevant information to the large and spatially consistent framework of well dated, high resolution Holocene climate archives available in the Mediterranean area (e.g., Roberts et al., 2008; Giraudi et al., 2011b). Comparison of the fragmentary Holocene record with the more continuous Eemian record in Fucino, enables us to assess that all the proxies probably oscillated in the same range of values during these two interglacials, possibly with deeper lake levels during the Holocene. To this point, we observe at least two marked lake shallowing events during the Holocene, one just after the deposition of TF-1 (modelled age 9.2 ± 0.5 ka) and one at ca. 2 ka (Figs. 7 and 9; cf. Giraudi, 1999). This latter lake shallowing can be consistently correlated with the construction of the Roman draining tunnel completed under emperor Claudius (year 52 C.E., Pliny the Elder, 78; Tacitus, 120; Svetonius, 122) which remained active until the collapse of the Western Roman Empire (year 476 C.E.; cf. Giraudi, 1999).

5. Conclusions

We have presented the new F1-F3 multi-proxy, high resolution record, documenting orbital to millennial-centennial scale environmental changes in the Mediterranean region with a robust radioisotopically-based chronology spanning over the last two glacial-interglacial cycles. Moreover, the F1-F3 records provides a robust assessment of age uncertainties and several tephrostratigraphic markers which can be used to align and synchronise different archives at a regional to extra regional scale. Our multi-proxy record indicates that different proxies show a wide range of environmental responses arising from the interaction between changes in lake level, reflecting changes in the local hydrological balance, and changes in the clastic input, as well as processes of soil erosion and glaciers development over the Apennines.

The F1-F3 record shows that this complex interplay of local environmental processes is strongly influenced by orbital parameters, especially during times of small to intermediate global ice volumes. The protracted process of environmental reorganization at the end of the Saalian glaciation seems to be in phase with obliquity. This might suggest that obliquity controlled mid-latitudes environmental processes also at times of large ice volume. In speculation, it can be proposed that such an early response of mid-latitudes to orbital forcing might have sustained the upcoming glacial termination and the abrupt onset of the Last Interglacial (LIG) maximum.

Our data show that the LIG maximum had a duration of about one half of a precession cycle, suggesting that precession had a fundamental role in supporting peak interglacial conditions. Prominent sub-orbital scale oscillations increasing in amplitude from the Eemian to the early Weichselian with terrestrial ecosystem oscillating around an “interglacial” state are also documented by the F1-F3 record. This suggests that, under intermediate global ice volumes, climatic shifts (although large) did not exceed the local environmental tolerance-resilience threshold. Conversely, during the Saalian and Weichselian glacial periods we observe a subdued sub-orbital scale variability with ecosystems operating in a strictly ruled glacial environment. This suggest that, during periods of large global ice volume, warming events were not able to fully sustain environmental recovery. In the presence of relatively large glacial-periglacial landforms in the catchment basin, pedogenesis and vegetation recovery were inhibited and even small temperature reductions were able to reactivate erosive processes restarting a transition to a barren environment.

Finally, on a wider methodological perspective, our research suggests that a cautionary approach should be used in correlating events as expressed in different archives. This is particularly true when considering proxies for different environmental processes whose underlying temporal relationships can be much more complex than assumed *a priori*. Further caution is also demanded by the limited knowledge of catchment evolution of most part of the lacustrine basin cited in the present manuscript, hindering the detection of possible non-climatic variation in local hydrography. All this strengthens the need for robust and independent chronologies to correctly understand climate induced environmental changes and related interplaying mechanisms.

Acknowledgements

This work was developed in the frame of the PhD project of Giorgio Mannella (XXXII cycle of the *Dottorato Regionale Pegaso* in Earth Sciences) and was funded by the University of Pisa ("*Progetto Ateneo*" 2017, leader G. Zanchetta) and MIUR (PRIN-2017, "FUTURE" project, leader G. Zanchetta). The authors want to thank the Quaternary Geology team of the Institute of Geology and Mineralogy, University of Cologne (Germany) for their valuable support in preliminary core handling and sample analysis. Authors are indebted to the open source community for providing the numerous tools and systems on which this research depends. Finally, we would like to thank the two anonymous reviewers for their thoughtful and constructive comments which improved the manuscript.

Appendix A. Supplementary data

Supplementary data to this article can be found online at https://doi.org/10.1016/j.quascirev.2019.02.032.

References

Albert, P.G., Tomlinson, E.L., Lane, C.S., Wulf, S., Smith, V.C., Coltelli, M., Keller, J., Lo Castro, D., Manning, C.J., Müller, W., Menzies, M.A., 2013. - Late glacial explosive activity on Mount Etna: implications for proximal–distal tephra correlations and the synchronisation of Mediterranean archives. J. Volcanol. Geotherm. Res. 265, 9–26.

Bar-Matthews, M., Ayalon, A., Kaufman, A., 2000. Timing and hydrological conditions of Sapropel events in the Eastern Mediterranean, as evident from speleothems, Soreq cave, Israel. Chem. Geol. 169 (1–2), 145–156.

Beierle, B.D., Lamoureux, S.F., Cockburn, J.M., Spooner, I., 2002. A new method for visualizing sediment particle size distributions. J. Paleolimnol. 27 (2), 279–283.

Blaauw, M., Christen, J.A., 2011. Flexible palaeoclimate age-depth models using an autoregressive gamma process. Bayesian analysis 6 (3), 457–474.

Boretto, G., Zanchetta, G., Ciulli, L., Bini, M., Fallick, A.E., Lezzerini, M., Andre, C., Colonese, A.C., Zembo, I., Trombino, L., Regattieri, E., Sarti, G., 2017. The loess deposits of Buca dei Corvi section (central Italy): revisited. Catena 151, 225–237.

Bosi, C., Galadini, F., Messina, P., 1995. Stratigrafia plio-pleistocenica della conca del Fucino. Il Quat. 8 (1), 83–94.

Boyle, J.F., 2000. Rapid elemental analysis of sediment samples by isotope source XRF. J. Paleolimnol. 23 (2), 213–221.

Brauer, A., Allen, J.R., Mingram, J., Dulski, P., Wulf, S., Huntley, B., 2007. Evidence for last interglacial chronology and environmental change from southern Europe. Proc. Natl. Acad. Sci. Unit. States Am. 104 (2), 450–455.

Cavinato, G.P., Carusi, C., Dall'Asta, M., Miccadei, E., Piacentini, T., 2002. Sedimentary and tectonic evolution of Plio–Pleistocene alluvial and lacustrine deposits of Fucino Basin (central Italy). Sediment. Geol. 148 (1–2), 29–59.

Civetta, L., Orsi, G., Pappalardo, L., Fisher, R.V., Heiken, G., Ort, M., 1997. Geochemical zoning, mingling, eruptive dynamics and depositional processes - the Campanian Ignimbrite, Campi Flegrei caldera, Italy. J. Volcanol. Geotherm. Res. 75 (3), 183–219.

Deino, A., Potts, R., 1992. Age-probability spectra for examination of single-crystal $^{40}Ar/^{39}Ar$ dating results: examples from Olorgesailie, southern Kenya Rift. Quat. Int. 13, 47–53.

Deino, A.L., Scott, G.R., Saylor, B., Alene, M., Angelini, J.D., Haile-Selassie, Y., 2010. $^{40}Ar/^{39}Ar$ dating, paleomagnetism, and tephrochemistry of Pliocene strata of the hominid-bearing Woraso-Mille area, west-central Afar Rift, Ethiopia. J. Hum. Evol. 58, 111–126.

Di Roberto, A., Smedile, A., Del Carlo, P., De Martini, P.M., Iorio, M., Petrelli, M., Pantosti, D., Pinzi, S., Todrani, A., 2018. Tephra and cryptotephra in ā 60,000-year-old lacustrine sequence from the Fucino Basin: new insights into the major explosive events in Italy. Bull. Volcanol. 80 (3), 20.

Dorale, J.A., Edwards, R.L., Alexander, E.C., Shen, C.C., Richards, D.A., Cheng, H., 2004. Uranium-series dating of speleothems: current techniques, limits, & applications. In: Studies of Cave Sediments. Springer, Boston, MA, pp. 177–197.

Drysdale, R.N., Zanchetta, G., Hellstrom, J.C., Fallick, A.E., Zhao, J.X., Isola, I., Bruschi, G., 2004. Palaeoclimatic implications of the growth history and stable isotope ($\delta^{18}O$ and $\delta^{13}C$) geochemistry of a Middle to Late Pleistocene stalagmite from central-western Italy. Earth Planet. Sci. Lett. 227 (3–4), 215–229.

Drysdale, R.N., Zanchetta, G., Hellstrom, J.C., Fallick, A.E., Zhao, J.X., 2005. Stalagmite evidence for the onset of the Last Interglacial in southern Europe at 129 ± 1 ka. Geophys. Res. Lett. 32 (24).

Drysdale, R.N., Zanchetta, G., Hellstrom, J.C., Fallick, A.E., McDonald, J., Cartwright, I., 2007. Stalagmite evidence for the precise timing of North Atlantic cold events during the early last glacial. Geology 35 (1), 77–80.

Drysdale, R.N., Hellstrom, J.C., Zanchetta, G., Fallick, A.E., Goñi, M.F., Couchoud, I., McDonald, R.M., Lohmann, G., Isola, I., 2009. Evidence for obliquity forcing of glacial termination II. Science 325 (5947), 1527–1531.

Fedele, F.G., Giaccio, B., Isaia, R., Orsi, G., 2003. The campanian ignimbrite eruption, Heinrich event 4, and palaeolithic change in Europe: a high-resolution investigation. Volcanism and the Earth's Atmosphere 301–325.

Fletcher, W.J., Goñi, M.S., Peyron, O., Dormoy, I., 2010. Abrupt climate changes of the last deglaciation detected in a Western Mediterranean forest record. Clim. Past 6 (2), 245–264.

Follieri, M., Magri, D., Sadori, L., 1989. Pollen stratigraphical synthesis from valle di Castiglione (roma). Quat. Int. 3, 81–84.

Francke, A., Wagner, B., Just, J., Leicher, N., Gromig, R., Baumgarten, H., Vogel, H., Lacey, J.H., Sadori, L., Wonik, T., Leng, M.J., Zanchetta, G., Sulpizio, R., Giaccio, B., 2016. Sedimentological processes and environmental variability at Lake Ohrid (Macedonia, Albania) between 637 ka and the present. Biogeosciences 13, 1179–1196.

Freda, C., Gaeta, M., Karner, D.B., Marra, F., Renne, P.R., Taddeucci, J., Scarlato, P., Christensen, J.N., Dallai, L., 2006. Eruptive history and petrologic evolution of the Albano multiple maar (Alban Hills, Central Italy). Bull. Volcanol. 68 (6), 567–591.

Freytet, P., Verrecchia, E.P., 2002. Lacustrine and palustrine carbonate petrography: an overview. J. Paleolimnol. 27 (2), 221–237.

Frezzotti, M., Giraudi, C., 1992. Evoluzione geologica tardo-pleistocenica ed olocenica del conoide complesso di Valle Majelama (Massiccio del Velino, Abruzzo). Il Quat. 5 (1), 33–50.

Galadini, F., Messina, P., 2004. Early–middle Pleistocene eastward migration of the abruzzi apennine (central Italy) extensional domain. J. Geodyn. 37 (1), 57–81.

Galli, P., Giaccio, B., Messina, P., Peronace, E., 2016. Three magnitude 7 earthquakes on a single fault in central Italy in 1400 years, evidenced by new palaeoseismic

results. Terra. Nova 28 (2), 146–154.
Genty, D., Blamart, D., Ouahdi, R., Gilmour, M., Baker, A., Jouzel, J., Van-Exter, S., 2003. Precise dating of Dansgaard–Oeschger climate oscillations in western Europe from stalagmite data. Nature 421 (6925), 833.
Genty, D., Combourieu-Nebout, N., Peyron, O., Blamart, D., Wainer, K., Mansuri, F., Ghaleb, B., Isabello, L., Dormoy, I., von Grafenstein, U., Bonelli, S., Landais, A., Brauer, A., 2010. Isotopic characterization of rapid climatic events during OIS3 and OIS4 in Villars Cave stalagmites (SW-France) and correlation with Atlantic and Mediterranean pollen records. Quat. Sci. Rev. 29 (19), 2799–2820.
Giaccio, B., Isaia, R., Fedele, F.G., Di Canzio, E., Hoffecker, J., Ronchitelli, A., Sinitsyn, A., Anikovich, M., Lisitsyn, S.N., Popov, V.V., 2008. The Campanian Ignimbrite and Codola tephra layers: two temporal/stratigraphic markers for the Early Upper Palaeolithic in southern Italy and eastern Europe. J. Volcanol. Geotherm. Res. 177 (1), 208–226.
Giaccio, B., Nomade, S., Wulf, S., Isaia, R., Sottili, G., Cavuoto, G., Galli, P., Messina, P., Sposato, A., Sulpizio, R., Zanchetta, G., 2012. The late MIS 5 Mediterranean tephra markers: a reappraisal from peninsular Italy terrestrial records. Quat. Sci. Rev. 56, 31–45.
Giaccio, B., Regattieri, E., Zanchetta, G., Wagner, B., Galli, P., Mannella, G., Niespolo, E., Peronace, E., Renne, P.R., Nomade, S., Cavinato, G.P., Messina, P., Sposato, A., Boschi, C., Florindo, F., Marra, F., Sadori, L., 2015a. A key continental archive for the last 2 Ma of climatic history of the central Mediterranean region: a pilot drilling in the Fucino Basin, central Italy. Sci. Drill. 20, 13.
Giaccio, B., Regattieri, E., Zanchetta, G., Nomade, S., Renne, P.R., Sprain, C.J., Drysdale, R.N., Tzedakis, P.C., Messina, P., Scardia, G., Sposato, A., Bassinot, F., 2015b. Duration and dynamics of the best orbital analogue to the present interglacial. Geology 43 (7), 603–606.
Giaccio, B., Niespolo, E.M., Pereira, A., Nomade, S., Renne, P.R., Albert, P.G., Arienzo, I., Regattieri, E., Wagner, B., Zanchetta, G., Gaeta, M., Galli, P., Mannella, G., Peronace, E., Sottili, G., Florindo, F., Leicher, N., Marra, F., Tomlinson, E.L., 2017a. First integrated tephrochronological record for the last~ 190 kyr from the Fucino Quaternary lacustrine succession, central Italy. Quat. Sci. Rev. 158, 211–234.
Giaccio, B., Hajdas, I., Isaia, R., Deino, A., Nomade, S., 2017b. High-precision ^{14}C and $^{40}Ar/^{39}Ar$ dating of the Campanian Ignimbrite (Y-5) reconciles the time-scales of climatic-cultural processes at 40 ka. Sci. Rep. 7, 45940.
Giraudi, C., 1988. Evoluzione geologica della piana del Fucino (Abruzzo) negli utlimi 30.000 anni. Il Quat. 1 (2), 131–159.
Giraudi, C., 1989. Lake levels and climate for the last 30,000 years in the Fucino area (Abruzzo-Central Italy) — a review. Palaeogeogr. Palaeoclimatol. Palaeoecol. 70 (1–3), 249–260.
Giraudi, C., 1990. Le variazioni di livello del Lago Fucino (Abruzzo) nel periodo 1783 – 1862: implicazioni climatiche. Il Quat. 3 (2), 167–174.
Giraudi, C., 1996. L'impronta del "Younger Dryas" degli "Heinrich Events" nell'evoluzione climatica e ambientale dell'Italia centrale. Il Quat. 9 (2), 533–540.
Giraudi, C., 1998. Late Pleistocene and Holocene lake-level variations in Fucino Lake (Abruzzo, central Italy) inferred from geological, archaeological and historical data. In: Harrison, S.P., Frenzel, B., Huckried, U., Weiss, M. (Eds.), Palaeohydrology as Reflected in Lake-Level Changes as Climatic Evidence for Holocene Times, vol. 25, pp. 1–17. Paläoklimaforschung.
Giraudi, C., 1999. Chronological assessment and palaeoenvironmental implications of the speleothems from the caves at the edge of Fucino Plain (Abruzzo, central Italy). Il Quat. 12 (1), 19–84.
Giraudi, C., 2012. The campo felice late Pleistocene glaciation (Apennines, central Italy). J. Quat. Sci. 27 (4), 432–440.
Giraudi, C., 2017. Climate evolution and forcing during the last 40 ka from the oscillations in Apennine glaciers and high mountain lakes, Italy. J. Quat. Sci. 32 (8), 1085–1098.
Giraudi, C., Frezzotti, M., 1997. Late Pleistocene glacial events in the central Apennines, Italy. Quat. Res. 48 (3), 280–290.
Giraudi, C., Giaccio, B., 2015. Middle Pleistocene glaciations in the Apennines, Italy: new chronological data and preservation of the glacial record. Geological Society, London, Special Publications 433 (1), 161–178.
Giraudi, C., Mussi, M., 1999. The central and southern Apennine (Italy) during OIS 3 and 2: the colonisation of a changing environment. Préhistorie Européenne 15, 113–121.
Giraudi, C., Bodrato, G., Lucchi, M.R., Cipriani, N., Villa, I.M., Giaccio, B., Zuppi, G.M., 2011a. Middle and late Pleistocene glaciations in the campo felice basin (central Apennines, Italy). Quat. Res. 75 (1), 219–230.
Giraudi, C., Magny, M., Zanchetta, G., Drysdale, R.N., 2011b. The Holocene climatic evolution of Mediterranean Italy: a review of the continental geological data. Holocene 21 (1), 105–115.
Giraudi, C., Zanchetta, G., Sulpizio, R., 2013. A Late-Pleistocene phase of Saharan dust deposition in the high Apennine mountains (Italy). Alpine and Mediterranean Quaternary 26 (2), 111–122.
Govin, A., Capron, E., Tzedakis, P.C., Verheyden, S., Ghaleb, B., Hillaire-Marcel, C., St-Onge, G., Stoner, J.S., Bassinot, F., Bazin, L., Blunier, T., Combourieu-Nebout, N., El Ouahabi, A., Genty, D., Gersonde, R., Jimenez-Amat, P., Landais, A., Martrat, B., Masson-Delmotte, V., Parrenin, F., Seidenkrantz, M.-S., Veres, D., Waelbroeck, C., Zahn, R., 2015. Sequence of events from the onset to the demise of the Last Interglacial: evaluating strengths and limitations of chronologies used in climatic archives. Quat. Sci. Rev. 129, 1–36.
Iorio, M., Liddicoat, J., Budillon, F., Incoronato, A., Coe, R.S., Insinga, D.D., Cassata, W.,S., Angelino, A., Tamburrino, S., 2014. Combined palaeomagnetic secular variation and petrophysical records to time-constrain geological and hazardous events: an example from the eastern Tyrrhenian Sea over the last 120 ka. Glob. Planet. Chang. 113, 91–109.
Isola, I., Ribolini, A., Zanchetta, G., Bini, M., Regattieri, E., Drysdale, R.N., Hellstrom, J.C., Bajo, P., Montagna, P., Pons-Branchu, E., 2019. Speleothem U/Th age constraints for the last glacial conditions in the apuan Alps, northwestern Italy. Palaeogeogr. Palaeoclimatol. Palaeoecol. 518, 62–71.
Köppen, W., 1918. Klassifikation der Klima nach Temperatur, Niederschlag und Jahreslauf. Petermanns Geogr. Mittl. 193–203.
Kylander, M.E., Ampel, L., Wohlfarth, B., Veres, D., 2011. High-resolution X-ray fluorescence core scanning analysis of Les Echets (France) sedimentary sequence: new insights from chemical proxies. J. Quat. Sci. 26 (1), 109–117.
Laskar, J., Robutel, P., Joutel, F., Gastineau, M., Correia, A.C.M., Levrard, B., 2004. A Long Term Numerical Solution for the Insolation Quantities of the Earth. http://vo.imcce.fr/insola/earth/online/earth/online/.
Laurenzi, M.A., Villa, I., 1987. $^{40}Ar/^{39}Ar$ chronostratigraphy of Vico ignimbrites. Period. Mineral. 56, 285–293.
Lee, J.Y., Marti, K., Severinghaus, J.P., Kawamura, K., Yoo, H.S., Lee, J.B., Kim, J.S., 2006. A redetermination of the isotopic abundances of atmospheric Ar. Geochem. Cosmochim. Acta 70, 4507–4512.
Lisiecki, L.E., Raymo, M.E., 2005. A Pliocene-Pleistocene stack of 57 globally distributed benthic δ18O records. Paleoceanography 20 (1).
Magny, M., de Beaulieu, J.L., Drescher-Schneider, R., Vannière, B., Walter-Simonnet, A.V., Millet, L., Bossuet, G., Peyron, O., 2006. Climatic oscillations in central Italy during the last glacial–holocene transition: the record from Lake accesa. J. Quat. Sci.: Published for the Quaternary Research Association 21 (4), 311–320.
Mannella, G., Giaccio, B., Zanchetta, G., Regattieri, E., Leicher, N., Scheidt, S., Grelle, T., Lehne, C., Rolf, C., Wonik, T., Nomade, S., Pereira, A., Niespolo, E., Renne, P., Leng, M.J., Dean, J., Thomas, C., Aritzegui, D., Gaeta, M., Florindo, F., Cavinato, G.P., Provenzale, A., Wagner, B., 2018. Fucino paleo-lake: towards the palaeoenvironmental history of the last 430 ka. Alpine and Mediterranean Quaternary 31, 137–141.
Martin-Puertas, C., Brauer, A., Wulf, S., Ott, F., Lauterbach, S., Dulski, P., 2014. Annual proxy data from Lago Grande di Monticchio (southern Italy) between 76 and 112 ka: new chronological constraints and insights on abrupt climatic oscillations. Clim. Past 10 (6), 2099–2114.
Martrat, B., Grimalt, J.O., Lopez-Martinez, C., Cacho, I., Sierro, F.J., Flores, J.A., Zahn, R., Canals, M., Curtis, J.H., Hodell, D., 2004. Abrupt temperature changes in the Western Mediterranean over the past 250,000 years. Science 306 (5702), 1762–1765.
Meyers, P.A., Ishiwatari, R., 1993. - Lacustrine organic geochemistry - an overview of indicators of organic matter sources and diagenesis in lake sediments. Org. Geochem. 20 (7), 867–900.
Meyers, P.A., Lallier-Vergès, E., 1999. Lacustrine sedimentary organic matter records of Late Quaternary paleoclimates. J. Paleolimnol. 21 (3), 345–372.
Meyers, P.A., Teranes, J.L., 2002. Sediment organic matter. In: Tracking Environmental Change Using Lake Sediments. Springer Netherlands, pp. 239–269.
Miccadei, E., D'Alessandro, L., Parotto, M., Piacentini, T., Raturlon, A., 2012a. Carta Geologica d'Italia Alla Scala 1:50.000 Foglio 378 "Scanno". http://www.isprambiente.gov.it/Media/carg/378_SCANNO/Foglio.html.
Miccadei, E., D'Alessandro, L., Parotto, M., Piacentini, T., Raturlon, A., 2012b. Note Illustrative Della Carta Geologica d"Italia Alla Scala 1:50.000 Foglio 378 "Scanno". http://www.isprambiente.gov.it/Media/carg/note_illustrative/378_Scanno.pdf.
Milner, A.M., Roucoux, K.H., Collier, R.E.L., Müller, U.C., Pross, J., Tzedakis, P.C., 2016. Vegetation responses to abrupt climatic changes during the last interglacial complex (marine isotope stage 5) at Tenaghi Philippon, NE Greece. Quat. Sci. Rev. 154, 169–181.
Müller, U.C., Pross, J., Tzedakis, P.C., Gamble, C., Kotthoff, U., Schmiedl, G., Wulf, S., Christanis, K., 2011. The role of climate in the spread of modern humans into Europe. Quat. Sci. Rev. 30, 273–279.
Narcisi, B., 2000. Late Quaternary eolian deposition in central Italy. Quat. Res. 54 (2), 246–252.
Niespolo, E.M., Rutte, D., Deino, A.L., Renne, P.R., 2017. Intercalibration and age of the alder Creek $^{40}Ar/^{39}Ar$ standard. Quat. Geochronol. 39, 205–213.
North Greenland Ice Core Project members, 2004. High-resolution record of Northern Hemisphere climate extending into the last interglacial period. Nature 7005 (431), 147–151.
Past Interglacials Working Group of PAGES, 2016. Interglacials of the last 800,000 years. Rev. Geophys. 54 (1), 162–219.
Parnell, A.C., Gehrels, W.R., 2015. Using chronological models in late Holocene sea-level reconstructions from saltmarsh sediments. In: Shennan, I., Long, A.J., Horton, B.P. (Eds.), Handbook of Sea-Level Research.
Paterne, M., Guichard, F., Duplessy, J.C., Siani, G., Sulpizio, R., Labeyrie, J., 2008. A 90,000–200,000 yrs marine tephra record of Italian volcanic activity in the Central Mediterranean Sea. J. Volcanol. Geotherm. Res. 177 (1), 187–196.
Plinius, G. S. "the Elder" (78) – Naturalis Historiae, Lib. XXXVI, s. 24.
Pollard, D., Barron, E.J., 2003. Causes of model–data discrepancies in European climate during oxygen isotope stage 3 with insights from the last glacial maximum. Quat. Res. 59 (1), 108–113.
R Core Team, 2016. R: A Language and Environment for Statistical Computing. R Foundation for Statistical Computing, Vienna, Austria. https://www.R-project.org/.
Rasmussen, S.O., Bigler, M., Blockley, S.P., Blunier, T., Buchardt, S.L., Clausen, H.B., Cvijanovic, I., Dahl-Jensen, D., Johnsen, S.J., Fischer, H., Gkinis, V., Guillevic, M.,

Hoek, W.Z., Lowe, J.J., Pedro, J.B., Popp, T., Seierstad, I.K., Steffensen, J.P., Svensson, A.M., Vallelonga, P., Vinther, B.M., Walker, M.J.C., Wheatley, J.J., Winstrup, M., 2014. A stratigraphic framework for abrupt climatic changes during the Last Glacial period based on three synchronized Greenland ice-core records: refining and extending the INTIMATE event stratigraphy. Quat. Sci. Rev. 106, 14–28.

Regattieri, E., Zanchetta, G., Drysdale, R.N., Isola, I., Hellstrom, J.C., Roncioni, A., 2014. A continuous stable isotope record from the penultimate glacial maximum to the Last Interglacial (159–121 ka) from Tana Che Urla Cave (Apuan Alps, central Italy). Quat. Res. 82 (2), 450–461.

Regattieri, E., Giaccio, B., Zanchetta, G., Drysdale, R.N., Galli, P., Nomade, S., Peronace, E., Wulf, S., 2015. Hydrological variability over the Apennines during the Early Last Glacial precession minimum, as revealed by a stable isotope record from Sulmona Basin, Central Italy. J. Quat. Sci. 30 (1), 19–31.

Regattieri, E., Zanchetta, G., Drysdale, R.N., Isola, I., Woodhead, J.D., Hellstrom, J.C., Giaccio, B., Greig, A., Baneschi, I., Dotsika, E., 2016. Environmental variability between the penultimate deglaciation and the mid Eemian: insights from Tana che Urla (central Italy) speleothem trace element record. Quat. Sci. Rev. 152, 80–92.

Regattieri, E., Giaccio, B., Nomade, S., Francke, A., Vogel, H., Drysdale, R.N., Perchiazzi, N., Wagner, B., Gemelli, M., Mazzini, I., Boschi, C., Galli, P., Peronace, E., 2017. A last interglacial record of environmental changes from the Sulmona Basin (central Italy). Palaeogeogr. Palaeoclimatol. Palaeoecol. 472, 51–66.

Renne, P.R., Balco, G., Ludwig, K.R., Mundil, R., Min, K., 2011. Response to the comment by W.H. Schwarz et al. on "Joint determination of ^{40}K decay constants and ^{40}Ar*/^{40}K for the Fish Canyon sanidine standard, and improved accuracy for ^{40}Ar/^{39}Ar geochronology" by PR Renne, et al. Geochem. Cosmochim. Acta 75, 5097–5100, 2010.

Renne, P.R., Sprain, C.J., Richards, M.A., Self, S., Vanderkluysen, L., Pande, K., 2015. State shift in Deccan volcanism at the Cretaceous-Paleogene boundary, possibly induced by impact. Science 350, 76–78.

Roberts, N., Jones, M.D., Benkaddour, A., Eastwood, W.J., Filippi, M.L., Frogley, M.R., Lamb, H.F., Leng, M.J., Reed, J.M., Stein, M., Stevens, L., Valero-Garcés, B., Zanchetta, G., 2008. Stable isotope records of Late Quaternary climate and hydrology from Mediterranean lakes: the ISOMED synthesis. Quat. Sci. Rev. 27 (25–26), 2426–2441.

Rosi, M., Vezzoli, L., Aleotti, P., De Censi, M., 1996. Interaction between caldera collapse and eruptive dynamics during the Campanian Ignimbrite eruption, Phlegraean Fields, Italy. Bull. Volcanol. 57 (7), 541–554.

Sadori, L., Koutsodendris, A., Panagiotopoulos, K., Masi, A., Bertini, A., Combourieu-Nebout, N., Francke, A., Kouli, K., Joannin, S., Mercuri, A.M., Peyron, O., Torri, P., Wagner, B., Zanchetta, G., Sinopoli, G., Donders, D.H., 2016. Pollen-based paleoenvironmental and paleoclimatic change at Lake Ohrid (south-eastern Europe) during the past 500 ka. Biogeosciences 13, 1423–1437.

Sánchez Goñi, M.F., Bard, E., Landais, A., Rossignol, L., d'Errico, F., 2013. Air–sea temperature decoupling in western Europe during the last interglacial–glacial transition. Nat. Geosci. 6 (10), 837.

Sinopoli, G., Masi, A., Regattieri, E., Wagner, B., Francke, A., Peyron, O., Sadori, L., 2018. Palynology of the last interglacial complex at Lake Ohrid: palaeoenvironmental and palaeoclimatic inferences. Quat. Sci. Rev. 180, 177–192.

Smith, V.C., Isaia, R., Pearce, N.J.G., 2011. Tephrostratigraphy and glass compositions of post-15 kyr Campi Flegrei eruptions: implications for eruption history and chronostratigraphic markers. Quat. Sci. Rev. 30 (25–26), 3638–3660.

Smith, V.C., Isaia, R., Engwell, S.L., Albert, P.G., 2016. Tephra dispersal during the Campanian Ignimbrite (Italy) eruption: implications for ultra-distal ash transport during the large caldera-forming eruption. Bull. Volcanol. 78 (6), 45.

Svetonius, G. T. (122) - De vita Caesarum – Divus Claudius, s. 20.

Syvitski, J.P. (Ed.), 2007. Principles, Methods and Application of Particle Size Analysis. Cambridge University Press.

Tacitus, P. C. (120) – Annales, Lib. XII, s. 56-57.

Tomassetti, B., Giorgi, F., Verdecchia, M., Visconti, G., 2003. Regional model simulation of the hydrometeorological effects of the Fucino Lake on the surrounding region. Ann. Geophys. 21 (11), 2219–2232.

Toucanne, S., Minto'o, C.M.A., Fontanier, C., Bassetti, M.A., Jorry, S.J., Jouet, G., 2015. Tracking rainfall in the northern Mediterranean borderlands during sapropel deposition. Quat. Sci. Rev. 129, 178–195.

Tzedakis, P.C., 2005. Towards an understanding of the response of southern European vegetation to orbital and suborbital climate variability. Quat. Sci. Rev. 24 (14–15), 1585–1599.

Waelbroeck, C., Labeyrie, L., Michel, E., Duplessy, J.C., McManus, J.F., Lambeck, K., Balbon, E., Labracherie, M., 2002. Sea-level and deep water temperature changes derived from benthic foraminifera isotopic records. Quat. Sci. Rev. 21 (1–3), 295–305.

Wilson, G.P., Reed, J.M., Frogley, M.R., Hughes, P.D., Tzedakis, P.C., 2015. Reconciling diverse lacustrine and terrestrial system response to penultimate deglacial warming in southern Europe. Geology 43 (9), 819–822.

Wulf, S., Hardiman, M.J., Staff, R.A., Koutsodendris, A., Appelt, O., Blockley, S.P., Lowe, J.J., Manning, C.J., Ottolini, L., Schmitt, A.K., Smith, V.C., Tomlinson, E., Vakhrameeva, P., Knipping, M., Kotthoff, U., Milner, A.M., Müller, U.C., Christanis, K., Kalaitzidis, S., Tzedakis, P.C., Schmiedl, G., Pross, J., 2018. The marine isotope stage 1–5 cryptotephra record of Tenaghi Philippon, Greece: towards a detailed tephrostratigraphic framework for the Eastern Mediterranean region. Quat. Sci. Rev. 186, 236–262.

Zanchetta, G., Regattieri, E., Giaccio, B., Wagner, B., Sulpizio, R., Francke, A., Vogel, H., Sadori, L., Masi, A., Sinopoli, G., Lacey, J.H., Leng, M.J., Leicher, N., 2016. Aligning and synchronization of MIS5 proxy records from Lake Ohrid (FYROM) with independently dated Mediterranean archives: implications for DEEP core chronology. Biogeosciences 13, 2757–2768.

Zanchetta, G., Bini, M., Giaccio, B., Manganelli, G., Benocci, A., Regattieri, E., Colonese, A.C., Boschi, C., Biagioni, C., 2017a. - Middle Pleistocene (MIS 14) environmental conditions in the central Mediterranean derived from terrestrial molluscs and carbonate stable isotopes from Sulmona Basin (Italy). Palaeogeogr. Palaeoclimatol. Palaeoecol. 485, 236–246.

Zanchetta, G., Bini, M., Isola, I., Regattieri, E., Ribolini, A., Sulpizio, R., 2017b. New findings of the campanian ignimbrite ash within slope deposits of the treska valley (F.Y.R.O.M). Italian Journal of Geoscience 136, 198–205.